



**HAL**  
open science

## Impact of the nature of the linker on the 2D and 3D organization of lipid-phenalenone conjugates

David Chapron, Jean-Philippe Michel, Arnaud Hemmerle, Philippe Fontaine, Jérémy Godard, Michel Goldmann, Frédérique Brégier, Vincent Sol, Véronique Rosilio

### ► To cite this version:

David Chapron, Jean-Philippe Michel, Arnaud Hemmerle, Philippe Fontaine, Jérémy Godard, et al.. Impact of the nature of the linker on the 2D and 3D organization of lipid-phenalenone conjugates. 2024. hal-04610629

**HAL Id: hal-04610629**

**<https://hal.science/hal-04610629v1>**

Preprint submitted on 13 Jun 2024

**HAL** is a multi-disciplinary open access archive for the deposit and dissemination of scientific research documents, whether they are published or not. The documents may come from teaching and research institutions in France or abroad, or from public or private research centers.

L'archive ouverte pluridisciplinaire **HAL**, est destinée au dépôt et à la diffusion de documents scientifiques de niveau recherche, publiés ou non, émanant des établissements d'enseignement et de recherche français ou étrangers, des laboratoires publics ou privés.

Public Domain

# **Impact of the nature of the linker on the 2D and 3D organization of lipid-phenalenone conjugates**

David Chapron<sup>1,5</sup>, Jean-Philippe Michel<sup>1,5</sup>, Arnaud Hemmerle<sup>2</sup>, Philippe Fontaine<sup>2</sup>, Jérémy Godard<sup>3</sup>, Michel Goldmann<sup>4,2</sup>, Frédérique Brégier<sup>3</sup>, Vincent Sol<sup>3,5</sup>, Véronique Rosilio<sup>1,5\*</sup>

<sup>1</sup> Université Paris-Saclay, CNRS, Institut Galien Paris-Saclay, 17 avenue des Sciences, 91400 Orsay, France.

veronique.rosilio@universite-paris-saclay.fr  
david.chapron@universite-paris-saclay.fr  
jean-philippe.michel@universite-paris-saclay.fr

<sup>2</sup> Synchrotron SOLEIL, L'Orme des Merisiers, Départementale 128, 91190 Saint-Aubin, France.

arnaud.hemmerle@synchrotron-soleil.fr  
philippe.fontaine@synchrotron-soleil.fr

<sup>3</sup> Univ. Limoges, LABCiS, UR 22722, 123 avenue Albert Thomas, 87000, Limoges, France.

jeremy.godard@unilim.fr  
frederique.bregier@unilim.fr  
vincent.sol@unilim.fr

<sup>4</sup> Institut des NanoSciences de Paris, CNRS, UMR 7588, Sorbonne Université, 4 place Jussieu, 75252 Paris cedex 05, France.

michel.goldmann@insp.jussieu.fr

<sup>5</sup> CNRS, GDR 2025 HappyBio, Université d'Orléans, 14 rue d'Issoudun, BP 6744, 45067 Orléans cedex 2, France.

\*To whom correspondence should be addressed.

## Abstract

A series of phenalenone-lipid conjugates (**1A**, **1B**, **1C**, **2**) have been synthesized to compensate for the poor water solubility of the photosensitizer phenalenone (PN) and promote the formation of nano-assemblies. We show that the organization and structure of monolayers upon compression strongly depend on the nature of the linker connecting PN to the lipid backbone, and the number of C<sub>18</sub> chains. Monolayer properties at the air-water interface were analyzed by surface pressure measurements, Brewster angle and atomic force microscopies, grazing incidence X-ray diffraction, and X-ray reflectivity. Whereas conjugate **1C** (ester bond) organizes into multilayers upon compression, conjugates **1A**, **1B**, and **2** form stable monolayers whose structure is controlled by van der Waals (vdW) interactions between C<sub>18</sub> chains, intermolecular H-bonding involving the linker, and for **1B**,  $\pi$ - $\pi$  stacking of PN moieties. Conjugate **1A** (amide-triazole linker) is structured into a rectangular network of chains with an order that extends only to the molecule of the adjacent cell. Conjugate **1B** (amide bond) forms two incommensurate networks, one for the chains and the other for the headgroups. The distance between molecules in the next near neighbor chain lattice and the sufficient degree of freedom of PN groups allows them to pile up via  $\pi$ - $\pi$  interactions below the chains in a rectangular cell. Conjugate **2** with its double chain adopts a similar behavior to that of a saturated phospholipid. Strong vdW interactions predominate and allow, at high surface pressure, hexagonal packing with no chain tilt. The distance between molecules prevents PN stacking. The identified PN derivative structures explain the linker's impact on the formation and stability of nano-assemblies.

**Keywords:** Photosensitizer; monolayer; Brewster Angle Microscopy; Atomic Force Microscopy; Grazing Incidence X-Ray Diffraction; X-Ray Reflectivity.

## 1. Introduction

Phenalenone (perinaphthenone, 1*H*-phenalen-1-one, PN) is a poorly water-soluble substance that has been extensively studied as a photosensitizer (PS) for antimicrobial activity [1-5]. Excitation of PN leads to type I or II reactions, producing either reactive oxygen species (ROS) or singlet oxygen, depending on whether PN is in aqueous or lipid media [6]. PN exhibits a singlet oxygen quantum yield close to unity in many solvents including water [7-9]. It is a better photosensitizer for producing singlet oxygen in a lipid medium than in an aqueous one [6]. This can be an advantage because the interaction of a PS with membranes is an efficient way to permeabilize them by photooxidation [10,11]. However, PN is hydrophobic and not surface active, which may limit its interaction with bacteria membranes [12]. Modifying the photosensitizer with lipid chains may promote its interaction with membranes. It may also allow the formation of nano-assemblies which ease the administration of hydrophobic photosensitizers and confer additional properties to them [13-15]. In previous work, we described the synthesis of four PN-lipid conjugates. In conjugates **1A**, **1B**, and **1C**, PN is covalently bound to a single saturated C<sub>18</sub> chain through an amide and a triazole groups, an amide bond, or an ester bond, respectively. In conjugate **2**, PN is conjugated to a diglyceride of stearic acid (Figure 1) [12].

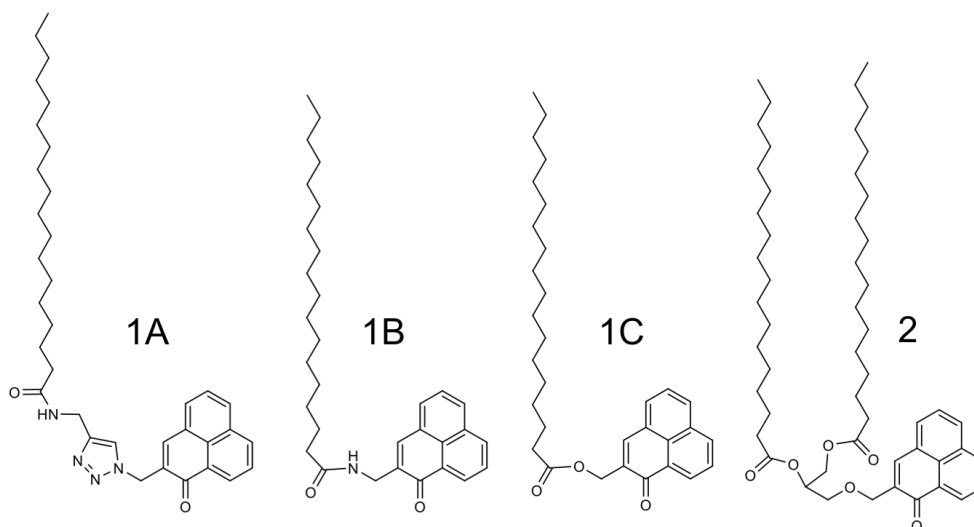


**Figure 1:** Chemical structure of the four studied PN derivatives.

We have analyzed the interfacial behavior of these conjugates at the air-water interface and observed that they formed monolayers in the liquid-condensed state (**1A**, **1B**), the liquid-expanded state (**1C**), or the solid state (conjugate **2**) [12]. Their molecular areas at collapse increased in the order  $1A < 1B-1C < 2$ , with values ranging from 0.20 to 0.35 nm<sup>2</sup>. All these values were lower than expected, considering the size of the PN molecule and the area of the cross-section of a fatty acid (0.20 nm<sup>2</sup>) or a phospholipid (0.48 nm<sup>2</sup> for distearoylphosphatidylcholine DSPC, with similar rigidity and lipid chain length as conjugate **2**) [16, 17]. Conjugates **1A**, **1B**, and **2** could form vesicles with a phospholipid, but these proved unstable with time, whatever the temperature at which they were formed [12, 18]. A thermodynamic study of PN derivatives mixtures with a phospholipid, including surface pressure and differential scanning calorimetry measurements, showed that conjugate **1A** was more disruptive to mixed monolayers than conjugate **1B**, and that this disruption was due to interactions between molecules in the plane of the interface rather than to interactions between lipid chains [18]. We thus hypothesized that the compounds interacted at the interface not only through van der Waals interactions at the level of lipid chains but also, possibly, via hydrogen bonding at the linker level, and  $\pi$ - $\pi$  interactions between PN molecules. For conjugate **2**, a grazing incidence x-ray diffraction (GIXD) experiment was performed with saturated and hybrid phospholipids which showed that the PN moiety interacted with phospholipid headgroups but did not indicate whether PN molecules were partially or fully immersed in the subphase [18].

It appeared that to better understand the behavior of PN derivatives in PN derivative-phospholipid mixtures, a more thorough analysis of the pure PN derivatives was necessary, which could allow answering questions like (i) how was PN positioned in the monolayers, partially between the acyl chains or below them, in the air or the water? (ii) how did the linker influence this positioning, as well as the structure of the monolayer? (iii) what interactions (van

der Waals,  $\pi$ - $\pi$ , hydrogen bonding) predominated for each PN derivative? and (iv) How did the interfacial behavior of the conjugates affect their self-assembling properties? With this intention, monolayers of the pure derivatives were analyzed by surface pressure measurements combined with Brewster angle microscopy (BAM), grazing incidence x-ray diffraction (GIXD), and x-ray reflectivity (XRR) at the air-water interface, and by atomic force microscopy (AFM) following monolayer transfer onto mica slides.

## 2. Material and Methods

### 2.1. Material

The N-((1-((1-oxo-1*H*-phenalen-2-yl) methyl)-1*H*-1,2,3-triazol-4-yl) methyl) stearamide (conjugate **1A**,  $M_w = 556.8$  g/mol), N-((1-oxo-1*H*-phenalen-2-yl) methyl) stearamide (conjugate **1B**,  $M_w = 475.7$  g/mol), (1-oxo-1*H*-phenalen-2-yl) methyl stearate (conjugate **1C**,  $M_w = 476.7$  g/mol) and the 3-((1-oxo-1*H*-phenalen-2-yl) methoxy) propane-1,2-diyl distearate (conjugate **2**,  $M_w = 817.3$  g/mol) were synthesized as previously described [12]. Chloroform and methanol (spectroscopic grade, >99.8% pure) were purchased from Carlo Erba. The ultrapure water was obtained using the Millipore Milli-Q<sup>®</sup> Direct 8 water purification System. Mica substrates with a surface area of  $1.5 \times 1.5$  cm<sup>2</sup> were used (Ted Pella Inc, Redding USA). Due to the plate-like structure composed of an octahedral alumina sheet sandwiched by two tetrahedral silicate sheets, freshly cleaved muscovite mica surfaces revealing a molecular smooth surface over micrometric areas were used for monolayer transfers.

### 2.2. Surface pressure measurements

Surface pressure-surface area ( $\pi$ -A) measurements were performed using a modified Lauda auto-recording Langmuir trough (MCN Lauda, Germany) enclosed in a plexiglas box, protected from light. All experiments were performed at  $22 \pm 1^\circ\text{C}$ . Before monolayer deposition, the

water subphase was cleaned by suction. The pure PN derivatives dissolved in a chloroform and methanol (9:1 v/v) mixture were spread at the air/water interface, and the system was left for 15 min to allow complete evaporation of the organic solvents. Monolayer compression was then performed at  $0.07 \text{ nm}^2 \cdot \text{molecule}^{-1} \cdot \text{min}^{-1}$  speed. Results are mean values of at least 3 measurements. Surface compressional moduli ( $C_s^{-1}$ ) of monolayers were calculated from the equation (1):

$$C_s^{-1} = - \left( A \frac{d\pi}{dA} \right)_T \quad (1)$$

where  $A$  is the molecular area, and  $d\pi$  the surface pressure change.

### *2.3. Brewster angle microscopy*

The morphology of the monolayers at various surface pressures was analyzed during film compression using a Brewster angle microscope (MicroBAM 3, NimaTechnology Ltd., Coventry, U.K.) connected to the auto-recording Langmuir trough. The microscope was equipped with a frequency laser diode ( $\lambda = 659 \text{ nm}$ , 30 mW optical power) generating a collimated beam of approximately 6 mm diameter, with a p-polarizer, analyzer, and a USB camera. The spatial resolution of the BAM was about 6  $\mu\text{m}$  per pixel, with a field of view of  $3.6 \times 4.1 \text{ mm}^2$ , resolved over  $640 \times 480$  pixels. Image size was  $4.0 \text{ mm}^2$  after rescaling.

### *2.4. Langmuir-Blodgett (LB) transfer of monolayers of phenalenone derivatives*

LB transfers of monolayers of PN derivative were performed at  $22^\circ\text{C}$  on freshly cleaved mica slides for analysis of the morphology of monolayers in the air by atomic force microscopy (AFM). PN derivative molecules were compressed at various surface pressures, after 20 min waiting time for the stabilization of the monolayers, LB transfer was performed by pulling out (under constant surface pressure at 1 mm/min) the mica surface that had been immersed in the

trough well prior to the spreading of the studied conjugates. The monolayer-covered mica slides were immediately transferred to the atomic force microscope (AFM) for analysis.

### *2.5. Atomic force microscopy experiments*

AFM experiments were performed using a JPK Nanowizard 3 UltraSpeed (JPK Instruments, Berlin, Germany) standing on an air-buffered table coupled to a dynamic anti-vibration device and enclosed in an acoustic box. AFM imaging was performed in AC mode (amplitude modulation) with gold-coated silicon nitride cantilever of 0.6 N/m nominal spring constant and 125-130 kHz resonance frequency (Bruker, Santa Barbara, USA). The pyramid-shaped tips had a radius of curvature around 20 nm. Images were taken at a scan rate of 1 Hz. Image processing (flatten, plane fit, edge and line detection) was performed with the JPK Data Processing software (JPK Instruments).

### *2.6. GIXD and XRR measurements*

Grazing Incidence X-Ray Diffraction (GIXD) and X-Ray Reflectivity (XRR) experiments were performed at the synchrotron SOLEIL, on the SIRIUS beamline [19]. In GIXD experiments, the incoming x-ray beam (8 keV,  $\lambda = 0.155$  nm) was vertically focalized and horizontally collimated to a  $0.1 \times 2$  mm<sup>2</sup> (vertical  $\times$  horizontal) spot and deflected downwards to impinge on the water surface at 2 mrad of incidence. Langmuir monolayers were prepared on water at 20°C in the Langmuir trough installed on the goniometer. The temperature inside the experimental hutch was  $21 \pm 1$ °C. Spectra were recorded at 0, 5, 15, 30 and 40 mN.m<sup>-1</sup> on a large Q-range ( $Q_{xy}$  12-22 nm<sup>-1</sup>, and  $Q_z$  0-8 nm<sup>-1</sup>). The scattered signal was measured using a Soller Slit collimator of 0.075° resolution and 2D Pilatus3 1M detector for GIXD measurements. On such a large  $Q_{xy}$  range, the background is made of the scattering of the incoming and reflected x-ray beam by the gaseous atmosphere, the diffuse scattering by the fluctuations of the air/water



interface, and by the correlation peak of the water layer illuminated by the x-ray beam at grazing incidence [20]. To describe this background, we used in the fitting procedure a linear decreasing function and a broad Gaussian function centered around  $19 \text{ nm}^{-1}$  with typically  $3 \text{ nm}^{-1}$  FWHM. On this function, one to four Lorentzian functions were added to describe the diffraction peaks. XRR experiments were performed with a beam size of (V×H)  $0.08 \times 2 \text{ mm}^2$  at 10 keV ( $\lambda = 0.124 \text{ nm}$ ). The measurements were conducted in an original geometry where the incidence angle on the last deflecting mirror of the SIRIUS beamline was varied to scan the incidence angle on the water surface ranging from 0 to  $2^\circ$ . This range corresponds to values of  $Q_z$  spanning from 0 to  $4 \text{ nm}^{-1}$ , providing sufficient coverage to capture the first oscillation characteristic of the reflectivity of a monolayer at the air-water interface. The upper limit of  $2^\circ$  on the water surface is determined by the reflectivity of the mirror. When the incidence angle on the mirror exceeds its critical angle of total external reflection, the intensity of the reflected x-ray intensity decreases significantly, and almost no x-rays are reflected from the mirror for angles greater than  $1^\circ$  on it, which is equivalent to an angle  $\theta$  of  $2^\circ$  on the water surface.

To ensure accurate normalization of the reflectivity curves, the intensity of the incident beam ( $I_0$ ) is monitored using an ionization chamber placed just before the liquid surface. In this specific geometry, as the incident angle increases, it is necessary to lower the liquid surface to accurately follow the deflection of the incident beam. The signal reflected by the interface is measured using a UFXC, a 2D x-ray detector with hybrid-pixel technology [21]. The detector is vertically moved to ensure that the reflected spot remains in a fixed position on the detector. For each data point on the reflectivity curve, the signal is measured by summing the intensities of pixels within a Region Of Interest (ROI) centered around the reflected beam. Background subtraction is then performed by calculating the average signal from ROIs located immediately above and below the ROI containing the reflected beam. Finally, to obtain the true reflectivity  $R$ , the signal is divided by a measurement of the direct beam on the detector, accompanied with

a proper normalization using the  $I_0$  intensity. The results are displayed conventionally as  $RQ_z^4$  plotted as a function of  $Q_z = \frac{4\pi}{\lambda} \sin \theta_z$ . This representation eliminates the influence of Fresnel reflectivity and enhances the visibility of oscillations in the data [22].

To compare with diffraction data, XRR measurements were conducted on replicates of the various monolayers at increasing surface pressures. The experimental XRR data were adjusted to a multilayer model using GenX 3.6 [23]. The model consisted of, from bottom to top, a semi-infinite layer of water, a layer of polar heads, and a layer of hydrocarbon chains. Through the fitting process, estimates for the thickness, density, and roughness of each layer were obtained. The limited resolution of the XRR data, with typically only one visible oscillation, did not allow for independent fitting of the chain and head layer thicknesses. While the total thickness of the layer is a robust parameter, the contribution of the head or the chain length is more intricate to recover. Consequently, whenever possible, constraints on the chain lengths issuing from GIXD results were put to restrain the parameter space. These results were condensed into an Electron Density Profile (EDP) expressed in electrons/nm<sup>3</sup> and normalized by the electron density of water (334 electrons/nm<sup>3</sup>). The uncertainties for each parameter in the XRR analysis were determined using the uncertainty determination tool of GenX, based on the likelihood function of parameters ensembles from Markov-chain Monte Carlo simulations, used here with the parameters: *samples* = 10000 and *burn* = 200.

### 3. Results and Discussion

#### 3.1. Organization and morphology of monolayers of single-chain lipid conjugates

The interfacial properties of conjugates **1A**, **1B**, and **1C** and the morphology of their monolayers are depicted in Figures 2-4 and S1-S3 and summarized in Table 1.

In systems where a lipid chain is conjugated to another molecule a change in the collapse molecular area and surface pressure is expected, due to the presence of the grafted molecule, immersed in the subphase, exposed to the air phase, or lying at the interface [24, 25]. The location of PN in conjugates monolayer is not obvious, because PN is not a hydrophilic molecule. Furthermore, different interactions may occur that can affect its positioning at the interface, like van der Waals interactions, intramolecular and intermolecular hydrogen bonding at the level of the linker, or  $\pi$ - $\pi$  stacking between PN molecules (favored or not by the linker). In previous work, we observed that the most voluminous and hydrophobic linker (amide + triazole, conjugate **1A**) led to the surface area closest to that of the stearic acid precursor, and that conjugate **1C** monolayers were more compressible than the others and collapsed at a much lower surface pressure (Table 1) [12, 26-29].

Table 1: Characteristics of the monolayers of stearic acid and phenalenone derivatives spread at the air/water interface. \*See Refs 26-29.

| <b>Conjugate</b>    | <b><math>A_{\text{onset}}</math> (nm<sup>2</sup>)</b> | <b><math>A_c</math> (nm<sup>2</sup>)</b> | <b><math>\pi_c</math> (mN/m)</b> | <b>Maximal <math>C_s^{-1}</math> (mN/m)</b> |
|---------------------|---|--|----------------------------------|---|
| <b>Stearic acid</b> | 0.25-0.30*  | 0.20-0.22*                               | 50-55*                           | 700-900*                                    |
| <b>1A</b>           | 0.45  | 0.20                                     | 37                               | 118   |
| <b>1B</b>           | 0.38  | 0.28                                     | 40                               | 223   |
| <b>1C</b>           | 0.44  | 0.26                                     | 15                               | 71  |
| <b>2</b>            | 0.69  | 0.34                                     | 57                               | 249   |

Contrarily to the amide bond in conjugate **1B**, the ester bond in conjugate **1C** is not expected to engage in hydrogen bonding [30], and the triazole suppresses the intramolecular hydrogen bonds and weakens the intermolecular ones that could be generated by the close amide bond in conjugate **1A** [18].

Brewster angle microscopy provides qualitative information about the different phases in monolayers at various surface pressures. Stearic acid is known to show a direct transition from gaseous to liquid-condensed phase, with the coexistence of both phases at low surface pressures [27]. The coexistence of a gas and liquid phase at zero surface pressure is also observed for the

three studied conjugates in which a PN molecule is linked to a C<sub>18</sub> chain. For conjugate **1A** in the gaseous phase, BAM images show a porous network with tens of micron-wide holes (Figure S1). Upon increasing the surface pressure, the pores disappear, and the monolayer contrast becomes uniform. At 20 mN/m, the monolayer is in the liquid-condensed state [18]. Collapse ripples are visible at 40 mN/m. For conjugate **1B** in the gaseous phase (Figure S2), domains with bright contrast appear and grow in size upon compression. At a molecular area close to 0.40 nm<sup>2</sup>, the domains coalesce. At higher surface pressure, the contrast becomes fully uniform. Compressibility moduli show that from 10 mN/m, the monolayer is in the liquid-condensed state [18]. For conjugate **1C** (Figure S3), BAM images also show the formation of large domains at zero pressure that gradually coalesce (around 15-16 mN/m). However, the monolayer remains in the liquid-expanded state. At 20 and 27 mN/m, the brighter BAM images tend to confirm the formation of 3D architectures as suggested by the increase in surface pressure in the  $\pi$ -A isotherms. BAM information allowed the selection of the surface pressures for monolayer transfer onto a solid substrate for AFM analysis.

AFM images of conjugate **1A** monolayers show at 15 and 30 mN/m the presence of stacked fibers or ripples with random orientation, uncorrelated with the dipping direction (Figure 2). Their height is 1.5 nm on average. Analysis of the average roughness of AFM pictures gives a value between 6 and 7 Å. Ripples have been generally reported for phospholipids or fatty acids in specific conditions [31-33]. However, rippled strands similar to those observed for conjugate **1A** were recently observed for pure hexadecyl nicotinate monolayers and attributed to repulsive dipole-dipole interactions [34]. The morphology of the monolayer may indicate the alignment of molecules, either in the same orientation (all chains on the same side) or in the opposite orientation. At low surface pressure, molecules could face each other with PNs  $\pi$ - $\pi$  stacked at the interface [12]. In this case, the short distance between PN molecules, imposed by  $\pi$ - $\pi$  stacking of phenalenone molecules could promote repulsive dipole-dipole interactions

comparable to those observed for hexadecyl nicotinate monolayers. At 30 mN/m, the morphology of the monolayers evolves. Bundles of conjugate **1A** fibers are formed (Figure 2 C-F) showing two levels of organization.

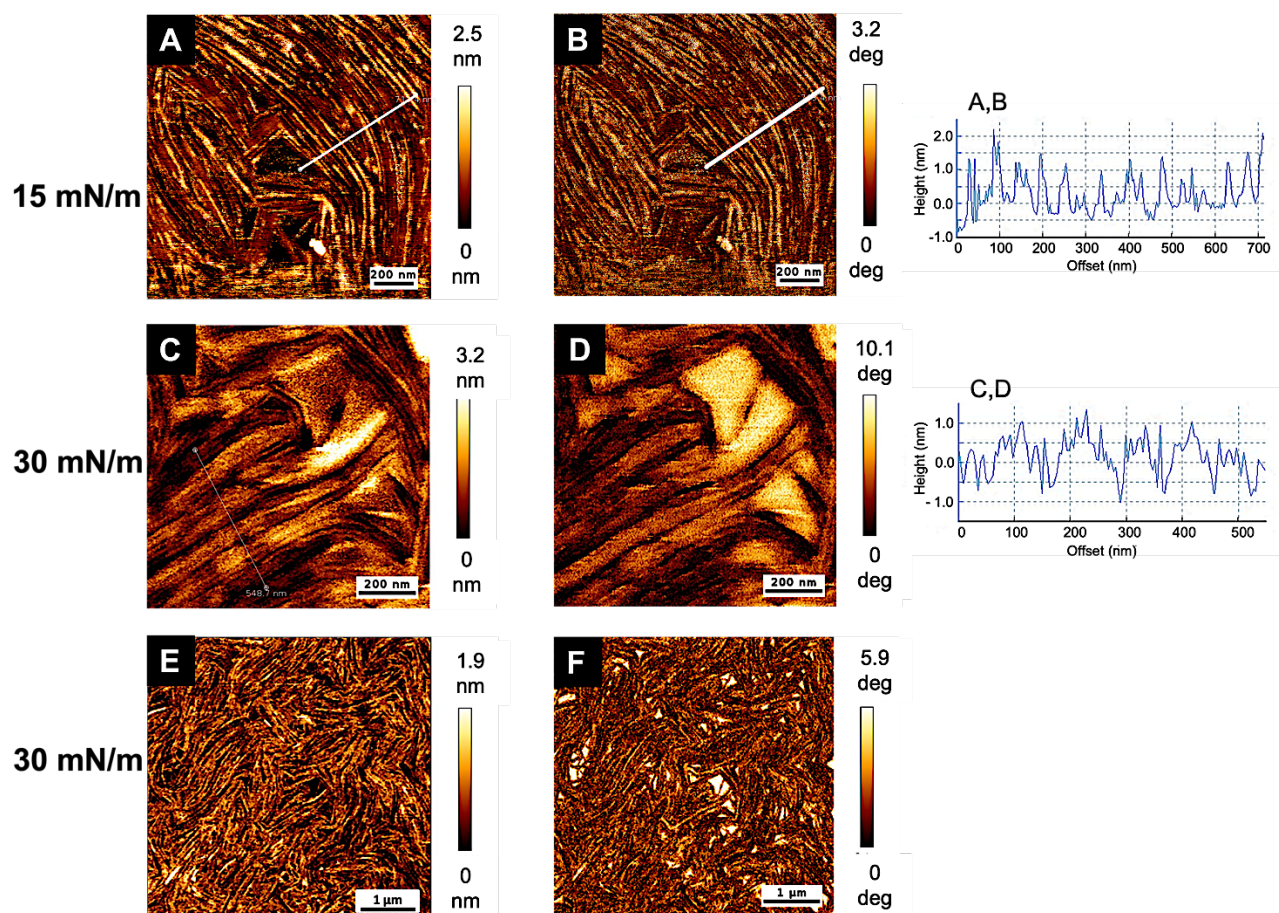


**Figure 2:** AFM height (A,C,E) and phase (B,D,F) images in the air of a monolayer of conjugate **1A** LB-transferred onto a mica slide. Scale bars = 200 nm (A-D) and 1  $\mu$ m (E,F). Corresponding height cross-sections are shown on the right.

For conjugate **1B**, LB-transfers were performed at 0, 1, and 30 mN/m. AFM images demonstrate that the monolayer is organized in roughly circular domains at the nanometer scale (Figure 3). Their shape is irregular but at 1 mN/m (D,E,F) and above (G,H,I), they grow in circular shapes and finally coalesce, although the contours of the domains remain visible at 30

mN/m. Their thickness is 1.5-2 nm, and their average roughness is 5 Å, corresponding to that expected for a monolayer.

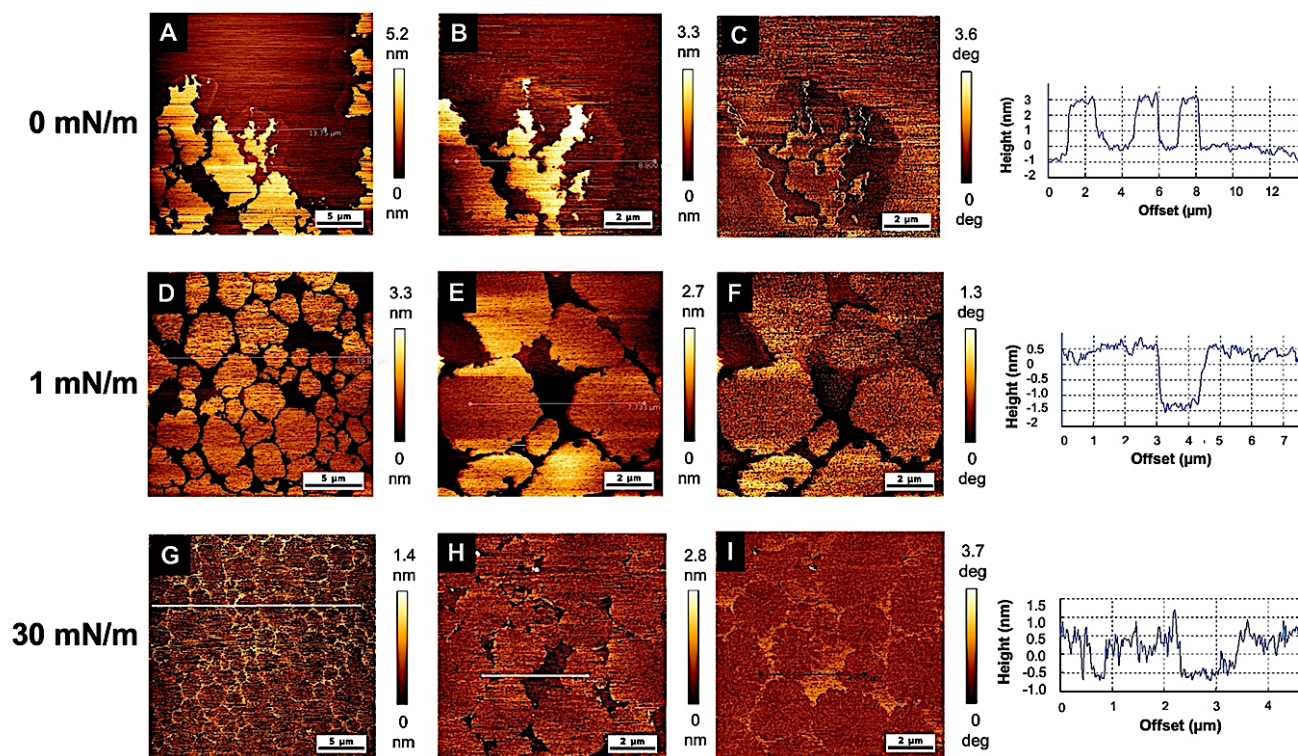


**Figure 3:** AFM height (A, B, D, E, G, H) and phase (C, F, I) images in the air of a monolayer of conjugate **1B**, LB-transferred onto a mica slide. Scale bars = 5 and 2  $\mu\text{m}$  for A,D,G and B,C,E,F,H,I, respectively. Height cross-sections are shown on the right.

For conjugate **1C**, AFM images in the air obtained after LB transfers at 15 and 30 mN/m are presented in Figure 4. The morphology of the layers does not show any specific organization. At 15 mN/m, the mean height of the domains is equal to 4 nm, corresponding to the formation of a bilayer. At 30 mN/m, a significant increase in height (up to 20-25 nm) accounts for the piling up of about 5 to 7 bilayers, confirming the collapse at about 15 mN/m and the formation of multilayers at higher surface pressures. The difference between conjugates **1B** and **1C** lies in the replacement of the amide bond by an ester bond. Compared to the O-CO bond, the N-CO bond is shorter and has a more intense barrier to rotation (partial double bond character)

which could reduce the freedom of the PN moiety relative to the acyl chain. This would be amplified by the propensity of the amide bond to get engaged in H-bonding. In conjugate **1C** monolayers, the PN molecules are less constrained and could interact more strongly, leading to the formation of multilayers, while conjugate **1B** forms rigid monolayers.

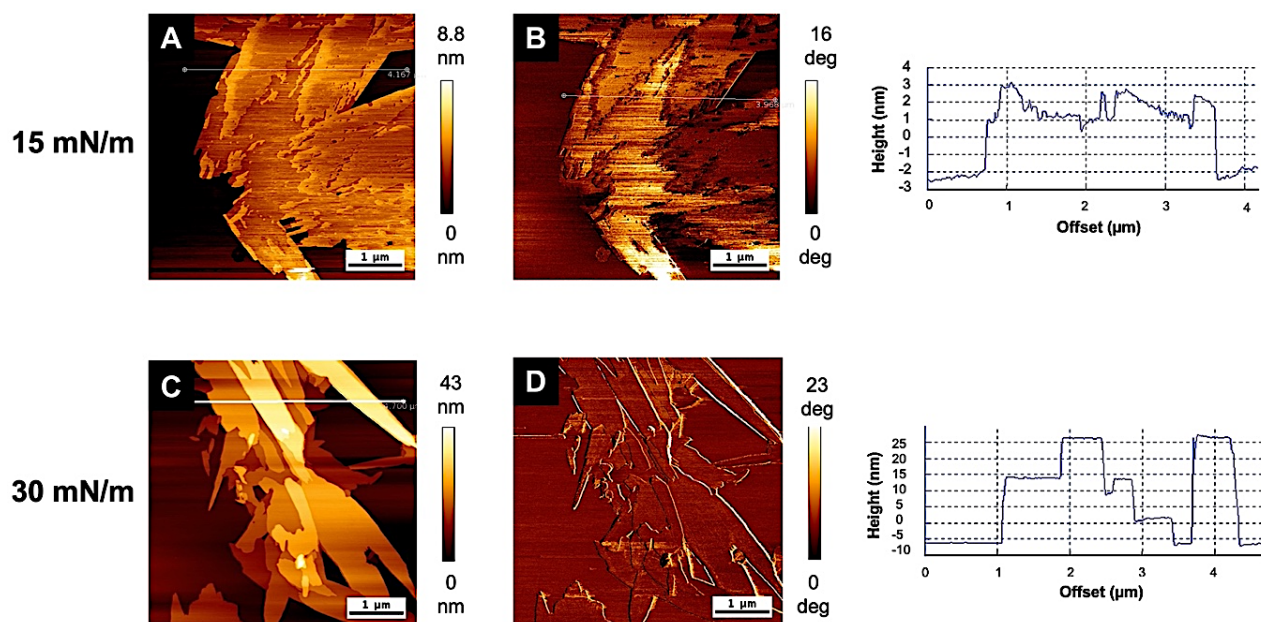


**Figure 4:** AFM height (A,C) and phase (B,D) images in the air of a conjugate **1C** monolayer LB-transferred onto a mica slide. Scale bar = 1 μm. Height cross-sections are shown on the right.

All these results show that PN derivatives resulting from the conjugation of a single C<sub>18</sub> chain organize differently at the interface depending on the nature of the linker used for the conjugation of PN to the lipid chain. Conjugate **1C** has a very low collapse surface pressure and compressibility moduli and its propensity to form multilayers makes it difficult to analyze its structure at the air-water interface. Thus, GIXD and XRR measurements were performed with conjugates **1A** and **1B** only.

### 3.2. Monolayer structure of the single-chain lipid conjugates

GIXD experiments by Dupres et al. revealed that a stearic acid monolayer is structured in a hexagonal lattice with a molecular axis perpendicular to the water surface and 0.477 nm intermolecular spacing [35]. Conjugate **1A** could generate a GIXD signal (Figure 5a-d, Table S1). The diffraction pattern is a very broad spectrum expanded at least over  $6 \text{ nm}^{-1}$ . The fitting procedure using Lorentzian functions describes this broad diffraction signal using two main peaks located at  $14.25 \text{ nm}^{-1}$  and  $15.44 \text{ nm}^{-1}$  (at 5 mN/m) as shown in Figure 5a and 5c and Table S1. A third small peak is necessary to account for a shoulder appearing on the lower  $Q_{xy}$  side of the diffraction signal. Figures 5 b-d show intensity maps  $I(Q_{xy}, Q_z)$  at  $20^\circ\text{C}$  for pure conjugate **1A** monolayer compressed at 5 and 30 mN/m. On these  $Q_{xy}$ - $Q_z$  maps, whereas the peak at  $14.25 \text{ nm}^{-1}$  exhibits a clear in-plane diffraction rod, the out-of-the-plane intensity distribution of the intensity seems more complex. Indeed, a clear out-of-the-plane maximum is present at  $Q_{xy} = 15.44 \text{ nm}^{-1}$  and  $Q_z = 4.15 \text{ nm}^{-1}$  corresponding to the  $[11]/[1\bar{1}]$  peak. It seems to belong to an arc of out-of-the-plane maximum intensity. This could be interpreted as a distribution of the acyl chain tilt in the monolayer around the mean value of  $15^\circ$ . This arc of intensity, when  $Q_z$  is integrated, could lead to a shoulder in the main diffraction peak at  $14.25 \text{ nm}^{-1}$  which does not correspond to a plain diffraction peak. This feature remains unchanged at all surface pressures. Considering only the two main peaks in the  $Q_{xy}$ - $Q_z$  map, the one at  $14.25 \text{ nm}^{-1}$  is in-plane whereas the one at  $15.44 \text{ nm}^{-1}$  is out-of-plane. If we index on a rectangular lattice the former one as  $[02]$  and the latter one as  $[11]$  and  $[1\bar{1}]$  (degenerated), such a diffraction spectrum corresponds to a rectangular arrangement of acyl chains tilted towards their nearest neighbors (NN) comparable to the L2 phase of the generic phase diagram of fatty acids or alcohol [36].

Analysis of the out-of-plane position of the  $[11]$  (or  $[1\bar{1}]$ ) peak indicates a tilt around  $15^\circ$  of conjugate **1A** acyl chains with respect to the normal to the interface which is insensitive to



surface pressure (Table S2). The full width at half maximum of the in-plane Bragg peaks (Table S1) corresponds to in-plane correlation lengths of 2-3 nm on average, indicating a very limited ordering that extends up to the first nearest neighboring molecules (Table S2). At higher  $Q_{xy}$  values, the deconvolution of the very broad peak did not allow us to confirm (or refute) PN stacking. Nevertheless, this stacking would be very limited.

XRR measurements performed on conjugate **1A** (Figure 5e-f, Table S3) showed a clear oscillation for pressures greater than 0 mN/m. Primary data analysis immediately indicates that the formed layer is rough, as evidenced by the quick decrease in reflectivity with  $Q_z$  values. The minimum in the oscillation evolves towards smaller  $Q_z$  vectors with increasing pressures, indicating a thickening of the layer. Quantitative results from the fit analysis show that the layer thickness of conjugate **1A** increased from 2.6 nm at 5 mN/m to 3.0 nm at 40 mN/m (Table S3) but with a particularly high roughness at each interface, around 0.8 nm. This value is consistent with the roughness deduced from AFM images (0.6-0.7 nm). This complicates further interpretation of the thickness in terms of head or tail components. Nevertheless, the XRR measurements clearly show that conjugate **1A** forms a single monolayer at the air/water interface. Among the three possible conformations for conjugate **1A**, conformations B and C are the most plausible (Figure 6).

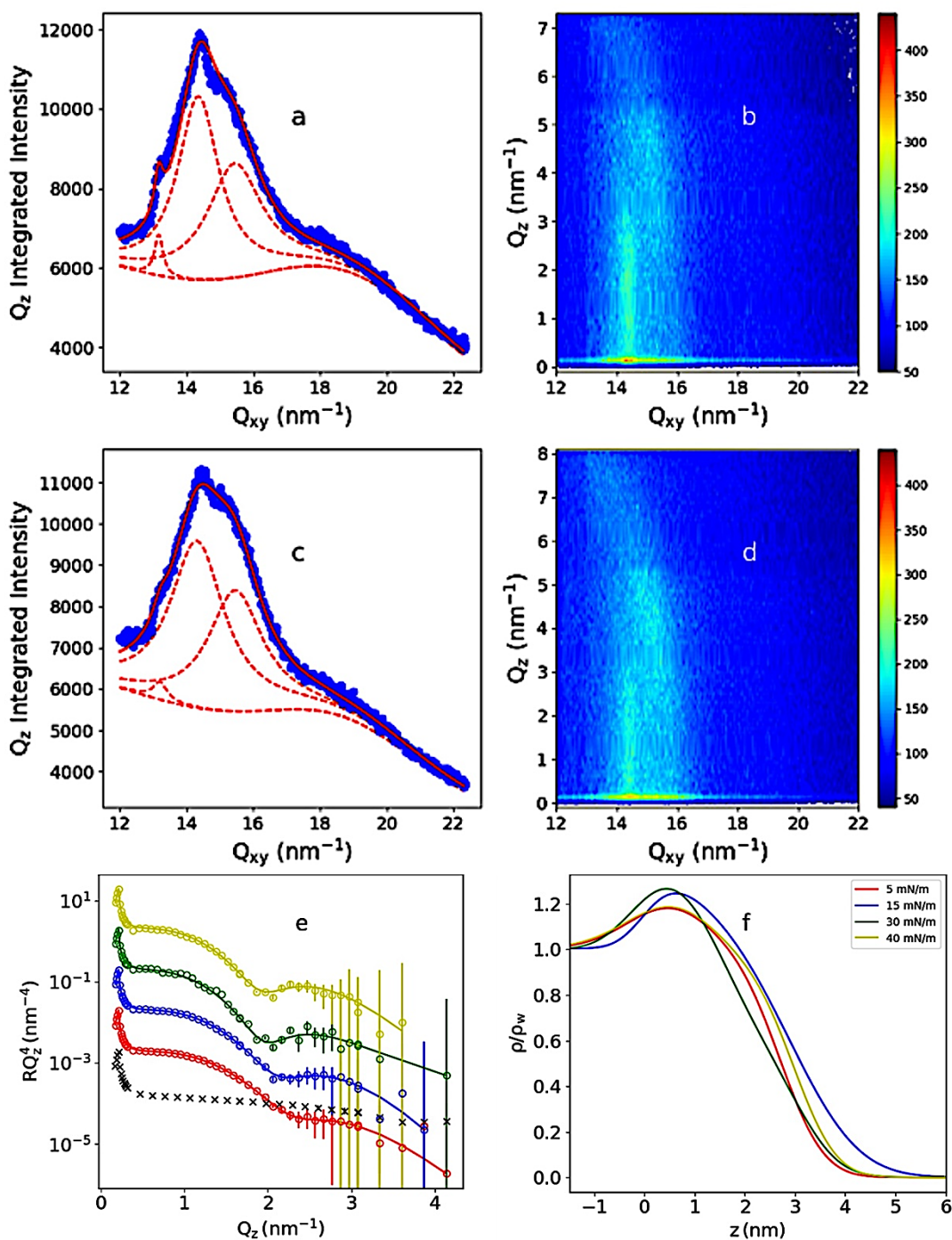


**Figure 5:** GIXD spectra for pure conjugate **1A** monolayer compressed at different surface pressures: (a) 5 mN/m, (c) 30 mN/m. Intensities are expressed after integration along  $Q_z$ . Experimental data: blue dots, fit: red line. Intensity maps  $I(Q_{xy}, Q_z)$  at 20°C for pure conjugate **1A** monolayer compressed at (b) 5 and (d) 30 mN/m on a water subphase. (e) Reflectivity data for conjugate **1A** (symbols, crosses for 0 mN/m and circles for higher pressures) and best fits associated (solid lines), normalized by the Fresnel reflectivity decrease in  $Q_z^{-4}$ . Data are shifted for clarity with increasing pressures, from bottom to top: 0, 5, 15, 30 and 40 mN/m. The electron density profiles normalized by the electron density of water ( $\rho_w$ ) are given in (f).

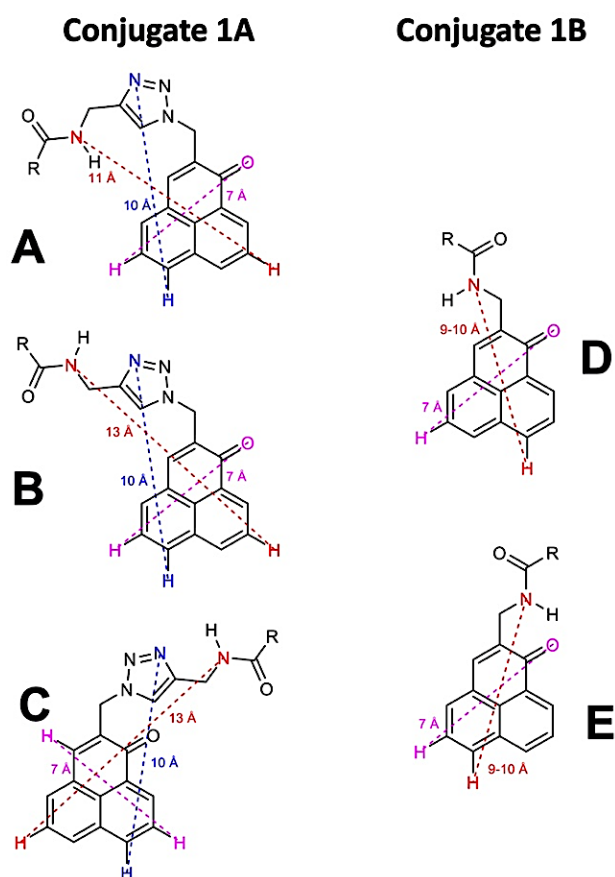


**Figure 6:** Possible conformations for conjugates **1A** and **1B** at the air-water interface. R = C<sub>18</sub>.

GIXD measurements performed on pure conjugate **1B** monolayer compressed at the air/water interface yielded a more complex diffraction pattern than that of conjugate **1A** (Figure 7 a-d). From surface pressures of 5 up to 41 mN/m, two distinct sets of Bragg peaks could be identified over a large  $Q_{xy}$  range (12-22 nm<sup>-1</sup>, Table S1). The first set was measured for  $Q_{xy}$  positions between 13.5 and 14.1 nm<sup>-1</sup>. As shown in Figures 7 a-d, these two peaks are measured whatever the surface pressure, and the spectrum is plotted as a  $Q_z$ -integrated spectra or a  $Q_{xy}$ - $Q_z$  intensity map. The latter representation provides evidence of the out-of-the-plane character of these peaks. Such diffraction spectrum is typical of diffraction by an aliphatic chain's assembly. If the lower  $Q_{xy}$  peak is indexed as [11] or [1 $\bar{1}$ ] (degenerated) and the higher  $Q_{xy}$  peak as [02], the spectrum corresponds to a centered rectangular structure with two chains per unit cell, of which  $a$  and  $b$  lattice parameters are reported in Table S2. The  $Q_z$  position of the [11]/[1 $\bar{1}$ ] and [02]

peaks are in a ratio of two. Such a configuration reveals a tilt of the chains towards their next nearest neighbors (NNN) which is similar to the L2' phase of long chain fatty acids or alcohol phase diagram [36].

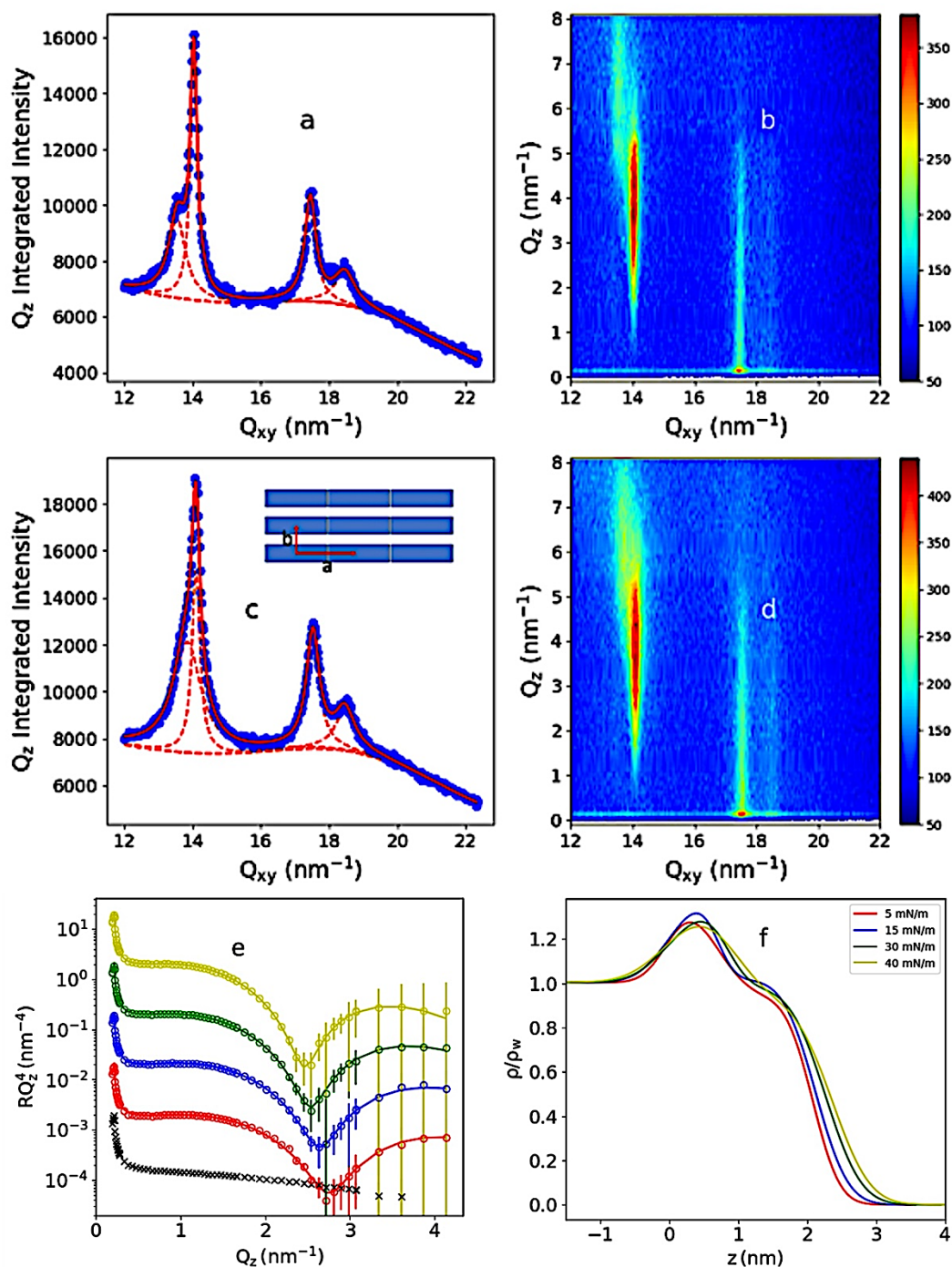


**Figure 7:** GIXD spectra for pure conjugate **1B** monolayer compressed at different surface pressures: (a) 5 mN/m, (c) 30 mN/m. Intensities are expressed after integration along  $Q_z$ . Experimental data: blue dots, fit: red line, individual contribution to the fit: dashed lines. Intensity maps  $I(Q_{xy}, Q_z)$  at 20°C for pure conjugate **1B** monolayer compressed at (b) 5 and (d) 30 mN/m on a water subphase. In the inset of (c), the top view sketch illustrates the structure of the PN headgroups. Blue rectangles with lattice vectors

represent PN molecules. (e) Reflectivity data for conjugate **1B** (symbols, crosses for 0 mN/m, and circles for higher pressures) and best fits associated (solid lines), normalized by the Fresnel reflectivity decrease in  $Q_z^{-4}$ . Data are shifted for clarity with increasing pressures, from bottom to top: 0, 5, 15, 30 and 40 mN/m. The corresponding normalized electron density profiles are given in (f).

Quantitative analysis of the out-of-plane position of the peaks indicates a significant tilt  $t$  ( $\sim 16^\circ$ ) of conjugate **1B** acyl chains with respect to the normal to the interface that does not evolve significantly with surface pressure (Table S2). The full width at half maximum of the in-plane Bragg peaks decreases with surface pressures (Table S1), and corresponds to in-plane correlation lengths of 15 nm on average (roughly 30 unit cells in the  $a$  direction and 15 in the  $b$  direction) (Table S2).

The second set holds on two other peaks located at positions  $17.45$  and  $18.58 \text{ nm}^{-1}$  and having slightly larger widths (Figure 7 a-c, Table S1). The intensity maximum appears in-the-plane as shown in the  $Q_{xy}$ - $Q_z$  intensity maps (Figures 7 b-d). This second set of diffraction peaks could be due to a phase separation between the NNN phase previously discussed and another phase with such diffraction signal. However, neither the surface pressure isotherms, nor the BAM images reveal any phase transition. Also, the peaks parameters are insensitive to surface pressure (Table S1). Finally, if we compute the distances corresponding to those peaks ( $2\pi/Q_{xy}$ ),  $0.36 \text{ nm}$ , and  $0.34 \text{ nm}$ , these distances are too short to correspond to a fatty acid chains assembly (if one considers them as first-order peaks). However, the  $0.36 \text{ nm}$  distance could correspond to PN stacking at the level of the polar head of the conjugate **1B**. Indeed, if we assume a rectangular structure as the one schematized in the inset of Figure 7c, where each rectangle stands for a PN moiety viewed in cross-section, we can index the first peak ( $\sim 17.45 \text{ nm}^{-1}$ ) as  $[02]$  and the second one ( $\sim 18.5 \text{ nm}^{-1}$ ) as  $[10]$ . Cell parameters associated with this lattice of phenalenones would be  $a = 0.34 \text{ nm}$  and  $b = 0.72 \text{ nm}$ , and the shorter distance ( $a$ ) of this lattice is close to the ideal distance ( $0.3$  to  $0.4 \text{ nm}$ ) between two PN moieties interacting through  $\pi$ - $\pi$

stacking [37]. The second distance ( $b$ ) corresponds to one of the diameters of the PN group that can be measured in conformation D and E (Figure 6).

The GIXD spectrum of conjugate **1B** displays features arising from the C<sub>18</sub> chains organized in a rectangular lattice with a given tilt, and the headgroup below, in which the PNs pile up in the monolayer through  $\pi$ - $\pi$  stacking, forming another rectangular lattice different from that of the chains. However, the area/chain is about 0.243 nm<sup>2</sup> as the maximum area/ headgroup is about 0.245 nm<sup>2</sup>, less than 1% larger than the chains one. The presence of these two lattices incommensurate between them could be explained by the different possible conformations of conjugate **1B** (Figure S4). The system can thus adopt a configuration where both parts of the molecule can organize to a certain extent. With the rectangular tilted NNN organization, acyl chains adopt a structure that enables the  $\pi$ - $\pi$  stacking of PN molecules. However, the incommensurate lattice of the headgroup organization results in a lower extent of the order. Especially in the  $a$  direction, the measured FWHM of the diffraction peak is 0.5 nm<sup>-1</sup> leading to a correlation length of 4 nm, much smaller than the correlation lengths of the chain lattice (larger than 10 nm).

To get better insight into the vertical structure of the layer and the possible formation of multilayers of conjugate **1B** during compression, XRR measurements were performed at the air-water interface (Figure 7 e-f, Table S3). At 0 mN/m, XRR data showed no oscillations, and the layer was not dense enough to be distinguished from the surface of pure water. A clear oscillation, characteristic of a monolayer, appeared in the measurements at higher surface pressures. The minimum of the curve shifted towards smaller  $Q_z$  vectors with increasing surface pressure, indicating a thickening of the monolayer. Indeed, the fits of reflectivity curves measured at different surface pressures provided a total thickness value of 2.09 nm at 5 mN/m increasing up to 2.37 nm at 40 mN/m (Table S3). The thickness and average roughness given by the AFM images were 1.5-2 nm, and 0.5 nm, respectively, in perfect agreement with XRR

results. They confirmed that conjugate **1B** forms a unique monolayer at the air/water interface, as deduced from AFM images obtained after LB transfer (Figure 3). By keeping the chain length constant while fitting the XRR data to varying pressures, in agreement with the stable chain tilt observed in GIXD, any thickness variation must stem from a change of conformation of the polar head. The polar head thickness increases from 0.66 nm at 5 mN/m up to 0.95 nm at 40 mN/m, a maximum value fully consistent with the N-H distance calculated in the two possible conformations D and E for conjugate **1B** (Figure 6). The Scattering Length Density (SLD) profiles extracted from the best fit of the XRR data are consistent with the positioning of PN moieties below the chain, in agreement with the results obtained from GIXD. The structure of the head groups and the distance between them leaves little space for the hydration of the system.

In conclusion, the GIXD and XRR results demonstrate that conjugate **1B** forms much more organized monolayers than those of conjugate **1A**. For the latter, no diffraction peaks appear at  $Q_{xy}$  higher than  $16 \text{ nm}^{-1}$ . The calculation of the dimensions of conjugates **1A** and **1B** indicates that conformation A in Figure 6 does not fit with GIXD and XRR data. Conversely, conformations B and C for conjugate **1A** and conformations D and E for conjugate **1B** are plausible. In these conformations, PN is positioned below the  $C_{18}$  chain. For **1A**, the high degree of freedom within the polar head group probably favors disorder and does not force the PN group to sit in a common plane, preventing  $\pi$ - $\pi$  interaction and stacking. Conversely, for conjugate **1B** the positioning and structure of the headgroups allow PN stacking.

### *3.3. Organization, morphology, and structure of the monolayers of the double-chain lipid conjugate*

Conjugate **2** exhibits a smaller molecular area and lower surface pressure at collapse than a phospholipid with two saturated C<sub>18</sub> chains like distearoylphosphatidylcholine (DSPC) [17], but similar maximal compressibility modulus. It forms a rigid monolayer. BAM images recorded during compression show domains with sharp edges at  $\pi = 0$  mN/m which merge at 1-5 mN/m. At 10 mN/m, the monolayer is in the liquid-condensed state. At 20 mN/m, it looks homogeneous. Collapse is detected above 50 mN/m. 3D aggregates appearing as bright lines are at the collapse (Figure S5). AFM images after transfer (Figure 8) demonstrate the presence of a porous monolayer at low surface pressures, similar to that of a phospholipid [38, 39]. Small dark circular domains with irregular shapes coexist with a surrounding homogeneous lighter matrix. They are many hundreds of nm wide and 2 nm deep on average. The domains appear to have some difficulties coalescing since at non-zero surface pressure the contour of the domains is still distinguished. The sharp edges suggest a high rigidity of the condensed phase and probably a high level of organization [39].



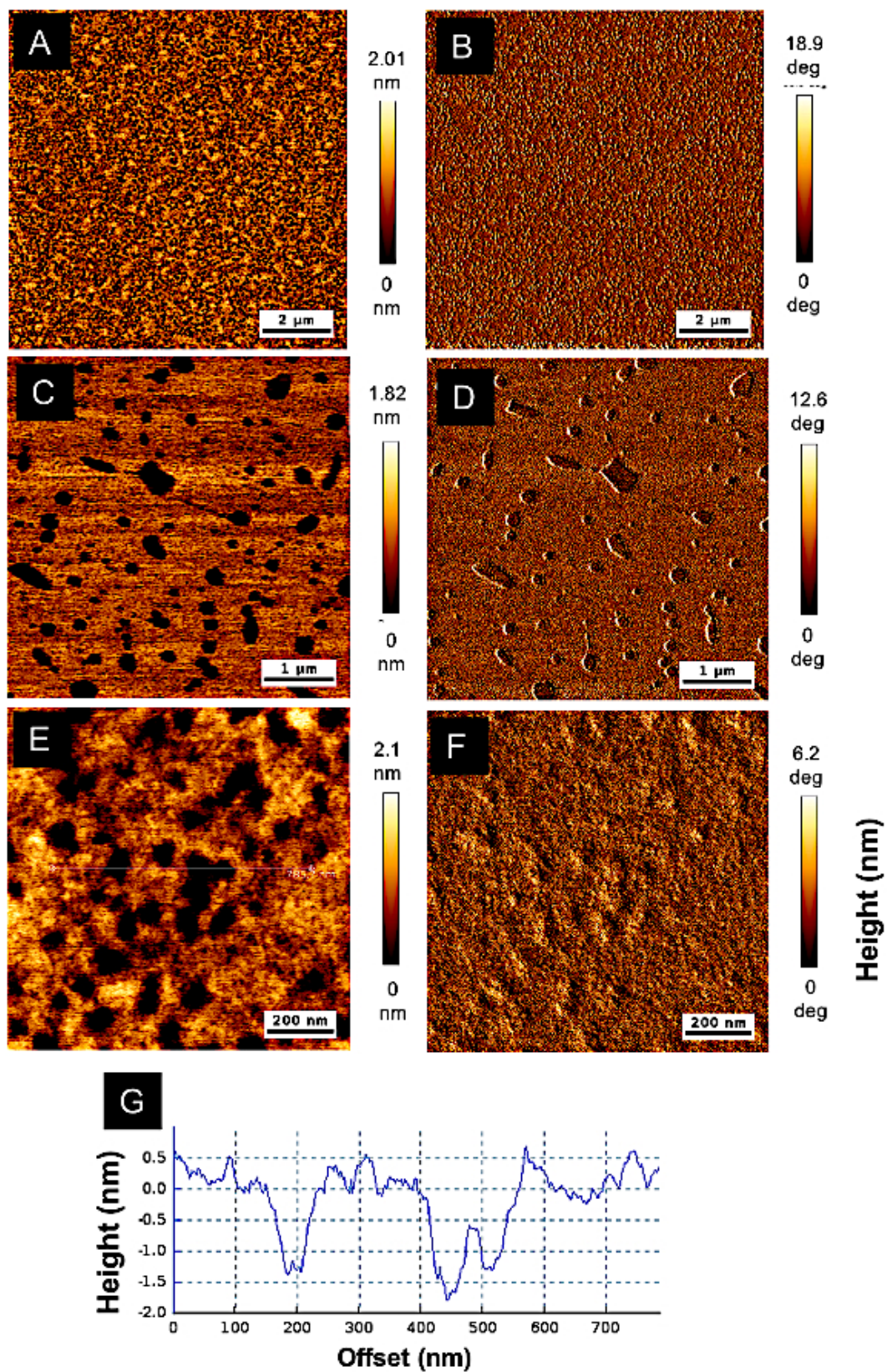


**Figure 8:** AFM height (left) and phase (right) images in the air of a conjugate **2** monolayer LB-transferred at 30 mN/m onto a mica slide. (A, B) scale bar = 2  $\mu\text{m}$ ; (C, D) scale bar = 1  $\mu\text{m}$ . (E,F) scale bar = 200 nm. (G) Height cross-sections from image (E).

Monolayers made of the pure conjugate **2** could diffract x-rays from 0 up to 45 mN/m (Figure 9 a-b, Table S1). Contrarily to conjugates **1A** and **1B**, only one single intense diffraction peak could be identified for non-null surface pressures at  $15.2 \text{ nm}^{-1}$  over a large  $Q$  range ( $12\text{-}22 \text{ nm}^{-1}$ ).

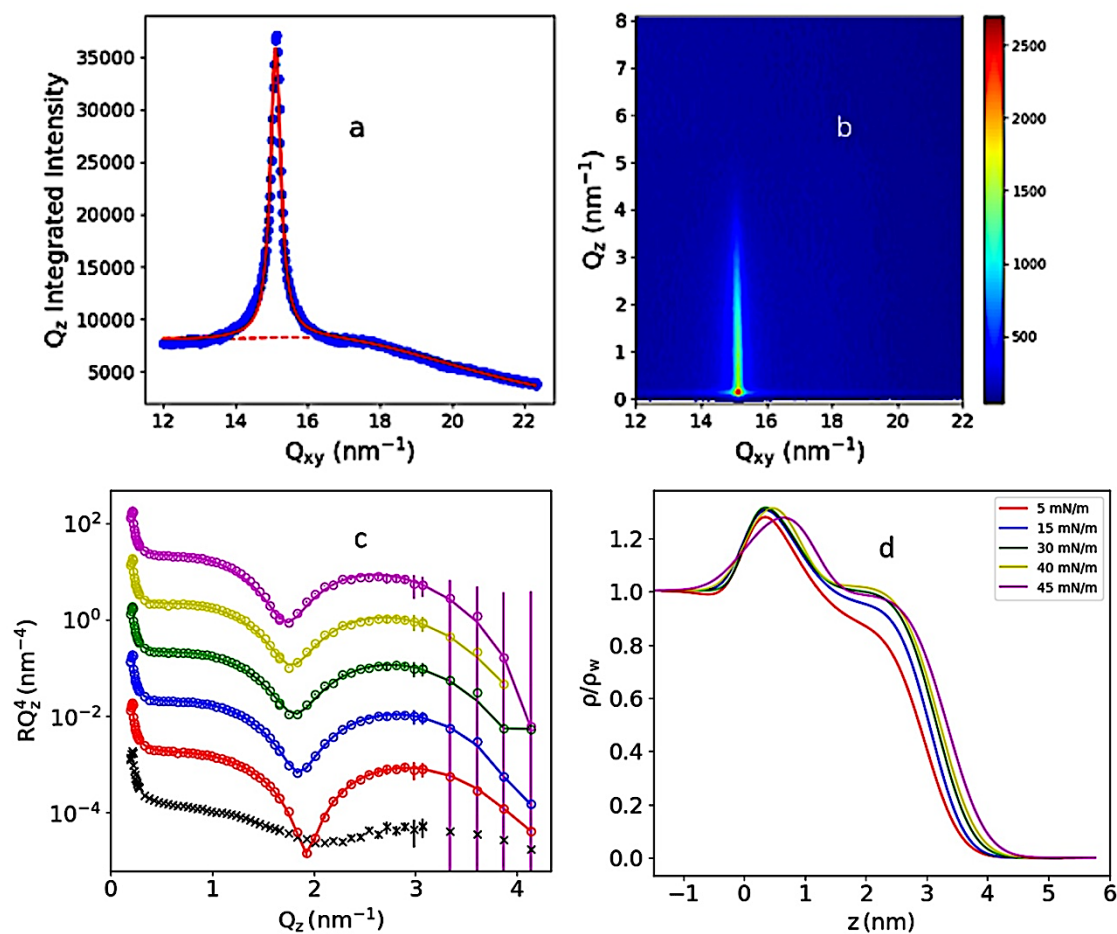


**Figure 9:** GIXD spectra for pure conjugate **2** monolayer compressed at 30mN/m and 20°C: **(a)**  $Q_z$ -integrated spectrum, Experimental data: blue dots, fit: red line. **(b)** Intensity maps  $I(Q_{xy}, Q_z)$  **(c)** Reflectivity data for conjugate **2** (symbols, crosses for 0 mN/m and circles for higher pressures) and best fits associated (solid lines), normalized by the Fresnel reflectivity decrease in  $Q_z^{-4}$ . Data are shifted for clarity with increasing pressures, from bottom to top: 0, 5, 15, 30, 40 and 45 mN/m. The corresponding normalized electron density profiles are given in **(d)**.

Such a unique, sharp, and intense peak is characteristic of a hexagonal packing of untilted acyl chains with a rather high correlation length. However, we choose to describe the structure with

a rectangular unit cell of which parameters are summarized in Table S2. These parameters appear insensitive to surface pressure confirming the highly compact arrangement of the acyl chains (about 0.18 nm<sup>2</sup>/chain). PN moieties do not stack significantly in the case of conjugate **2**. Indeed, the area per molecule, thus per PN molecules in a very compact arrangement of the chains, leads to a mean distance between PN molecules that is too large to enable stacking through  $\pi$ - $\pi$  interactions. XRR measurements indicate that conjugate **2** forms a unique monolayer at the interface (Figure 9 c,d). Even in the gaseous phase (0 mN/m), the layer is sufficiently dense to show a weak oscillation in XRR data that differs from an air-water interface. Again, the layer thickening with pressure can already be seen in the displacement of the minimum towards smaller  $Q_z$ , and the fits give a total thickness of 2.97 nm at 5 mN/m and 3.23 nm at 40 mN/m (Table S3, Figure S6). The roughness decreases significantly. As the tilt of the chains does not vary during compression, the increase in the total thickness can only be due to a rearrangement of the PN part in contact with water.

#### *3.4. Consequences of the properties of the lipid-phenalenone conjugates on the formation of nano-assemblies.*

The objective of forming nano-assemblies of lipid derivatives of phenalenone stems from the poor water solubility of this compound, which limits its administration. In previous works, we mentioned the difficulty of obtaining micelle-like nano-assemblies of pure conjugates **1A** and **1B**. We also showed that the pure conjugate **2** either formed ovoid multilamellar vesicles with undulated bilayers or large shapeless bilayer stacks [12, 18]. Although conjugates **1A** and **1B**, at molar fractions equal to or higher than 10 mol%, formed multi- or oligolamellar vesicles with stearyl oleoyl phosphatidylcholine (SOPC), the vesicles were not stable and turned to bilayer sheets and fibers (**1A**), or small unilamellar vesicles, bilayer sheets and stacks (**1B**) (Figure S7). When mixed with SOPC, conjugate **2** induced the breaking of the multilamellar phospholipid

vesicles into various small (size  $\leq 100$  nm) faceted unilamellar objects. At high concentration (50 mol%) these objects coalesced and evolved into nanodiscs approximately 100 nm in diameter and coexisted with conjugate **2**-rich ovoid multilamellar vesicles like those in Figure S7d [18].

The synthesis of lipid derivatives of photosensitizers capable of self-assembly is not new. Other PSs more hydrophobic than PN have been modified with lipid chains to form assemblies that facilitate their administration. However, these derivatives have well-defined polar headgroups [14]. In Figure S4, the schematic representation of possible orientations of conjugate **1B** shows that none of them allows the orientation of the polar groups towards the aqueous phase. The first of our initial questions concerned the positioning of the PN fraction at the interface. Our results reveal that when packed in a monolayer, the molecules of all conjugates are organized with PN under the chains in contact with the aqueous subphase but not necessarily fully immersed. This positioning of PN below the C<sub>18</sub> chain leads to the formation of complex lattices for **1A** and **1B** that prevent efficient packing for the formation of micelle-like systems and contribute to the destabilization of vesicles formed with SOPC. Another question concerned the propensity of PN to stack in monolayers and the consequence of this stacking on the stability of nano-assemblies. Our results show that the polymorphism of phospholipid-conjugate **1A** supramolecular assemblies is not due to PN stacking. GIXD results indicate that stacking over a few nm is only possible for conjugate **1B**. The structure of the head groups and the distance between them leaves little space for the hydration of the system.

Conjugate **2**, due to its two C<sub>18</sub> chains, shows a different behavior. It behaves like a saturated phospholipid. In previous work, we determined its phase transition temperature and attempted to form vesicles above this temperature [18]. However, the multilamellar vesicles obtained were still unstable, and the formation of bilayer stacks increased with the concentration of conjugate **2** in mixtures with the phospholipid. As GIXD and XRR results demonstrate for this compound

that PN molecules are in the water and that stacking is improbable in the plane of the interface, the observed stacking in multilamellar vesicles most probably originates from the interaction of PN molecules from two adjacent bilayers, leading to gradual vesicle destabilization. Some changes in the formulation of vesicles might allow overcoming this issue.

## Conclusion

In this work, we focused on the interfacial behavior and structure of the pure monolayers of phenalenone conjugated to one or two lipid chains *via* various linkers. The objective was to determine the positioning of PN in the monolayer, the influence of the linker on this positioning and the structure of the monolayer, the interactions involved and identify the predominant ones, and the effect of conjugates organization at the interface on their self-assembling properties. The determination of the structure of the monolayers allowed us to answer most questions.

(i) For all conjugates forming monolayers, the results indicate that PN molecules are positioned below the C<sub>18</sub> chains. GIXD experiments allowed us to identify plausible conjugate **1A** and conjugate **1B** conformations. Conjugate **2** behaves like a phospholipid at the interface.

(ii) The bulkiness and propensity of a linker to hydrogen bonding influence the positioning of PN. For conjugates **1A** and **2**, the bulky linkers favor immersion of the PN heads in water during compression. In the monolayers of conjugate **1A**, contradictory effects of the linkers' amide and triazole groups make hydrogen bonding unlikely. The partial double bond character of the amide linker in conjugate **1B** provides stabilizing H-bonds and added rigidity to the monolayer. The ester bond in conjugate **1C** is unable to engage in H-bonds, and less constrained PN molecules can interact more strongly, facilitating the formation of multilayers.

(iii) The fact that a factor 2 is observed between mean molecular areas of conjugates **1A** and **2** indicates that the acyl chains govern the interfacial behavior of both molecules and that the headgroup immersed in water does not influence it. This is confirmed by the identified

conformations for conjugate **1A**. The high degree of freedom within the polar head group probably favors disorder and does not force the PN group to sit in a common plane, preventing  $\pi$ - $\pi$  interaction and stacking. Conversely, PN participates in the interfacial behavior of conjugate **1B**: despite a rather constrained structure of the chains resulting from both hydrophobic interactions and H-bonding at the level of the linker, the PN head groups pile up via  $\pi$ - $\pi$  interactions under the chains in a rectangular cell. The structural determination by GIXD and XRR measurements *in situ* is consistent with PN stacking, imposing the organization for the head groups of conjugate **1B** in a lattice incommensurate to that of the acyl chains. The distance between molecules in the NNN tilted chain lattice leaves little space for the hydration of the system and the sufficient degree of freedom of the PN group enables  $\pi$ - $\pi$  interaction.

(iv) For all single chain-conjugate monolayers, the monolayer structure is defined as a rectangular unit cell with tilted chains. Conjugate **2** adopts a similar behavior to that of a saturated phospholipid. Its interfacial behavior is mainly controlled by the interactions between the double aliphatic chain, which allow, at high surface pressures, hexagonal packing with no chain tilt. PN molecules are immersed in water below the chains and the distance between them prevents their stacking. These features observed at surface pressures corresponding to the lateral pressure in vesicles are coherent with the ability of conjugate **2** to form vesicles when mixed with a phospholipid. Although lateral  $\pi$ - $\pi$  stacking is prevented, stacking of PN molecules from two adjacent bilayers is possible, leading to gradual vesicle destabilization and formation of nanodiscs, especially at high conjugate **2** molar fractions.

The results obtained highlight the importance of the choice of the linker for controlling the interfacial behavior and self-assembling properties of PN-lipid conjugates.

### **CRedit authorship contribution statement**

**DC:** Methodology, Investigation, Validation; **JPM:** Investigation, Formal analysis; **AH:** Methodology, Validation; **PF:** Methodology, Validation; **JG:** Resources; **MG:** Validation; **FB:** Resources; **VS:** Resources, Supervision; **VR:** Conceptualization, Methodology, Validation, Supervision, Writing, Review & Editing.

### **Declaration of Competing Interest**

The authors declare that they have no known competing financial interests or personal relationships that could have appeared to influence the work reported in this paper.

### **Data Availability**

The data presented in this study are available on request from the corresponding author.

### **Acknowledgments**

The authors would like to acknowledge SOLEIL for the provision of synchrotron radiation facilities and the use of SIRIUS Beamline in projects 20200096, 20210232, and 20220235. They also thank Dr. Sylvain Trepout (Institut Curie, Orsay, France) and Dr. Eric Larquet (CIMEX – Ecole Polytechnique, IP Paris, Palaiseau Cedex, France) for cryoTEM images and helpful discussions.

**Funding:** This research did not receive any specific grant from funding agencies in the public, commercial, or not-for-profit sectors.

**Supplementary information:** Interfacial behavior of single chain PN-conjugates **1A**, **1B** and **1C**; Possible conformations of conjugate **1B** at the air-water interface; Interfacial behavior of double chain PN-conjugate **2**; GIXD and XRR parameters for the pure conjugates **1A**, **1B** and **2**; Morphology of nano-assemblies made of conjugates **1A**, **1B** and **2**.

## References:

- [1] J. Godard, D. Gibbons, S. Leroy-Lhez, R.M. Williams, N. Villandier, T.-S. Ouk, F. Brégier, V. Sol, Development of phenalenone triazolium salt derivatives for aPDT: Synthesis and antibacterial screening, *Antibiotics*, 10 (2021a) 626.  
<https://doi.org/10.3390/antibiotics10060626>
- [2] C. Sandoval-Altamirano, J.R. De la Fuente, E. Berios, S.A. Sanchez, N. Pizarro, J. Morales, G. Gunther, Photophysical characterization of hydroxy and ethoxy phenalenone derivatives, *J. Photochem. Photobiol. A: Chem.* 353 (2018) 349-357.  
<https://doi.org/10.1016/j.jphotochem.2017.11.049>
- [3] M.C. Daza, M. Doerr, S. Salzmann, C.M. Marian, W. Thiel, Photophysics of phenalenone: quantum-mechanical investigation of singlet-triplet intersystem crossing, *Phys. Chem. Chem. Phys.* 11 (2009) 1688-1696. <https://doi.org/10.1039/b815724c>
- [4] J. Arnbjerg, M.J. Paterson, C.B. Nielsen, M. Jørgensen, O. Christiansen, P.R. Ogilby, One- and two-photon photosensitized singlet oxygen production: Characterization of aromatic ketones as sensitizer standards, *J. Phys. Chem. A*, 111 (2007) 5756-5767.  
<https://doi.org/10.1021/jp0711971>
- [5] C. Flors, S. Nonell, Light and singlet oxygen in plant defense against pathogens: Phototoxic phenalenone phytoalexins, *Acc. Chem. Res.* 39 (2006) 293-300.  
<https://doi.org/10.1021/ar0402863>
- [6] C. Espinoza, A. Trigos, M.E. Medina, Theoretical study on the photosensitizer mechanism of phenalenone in aqueous and lipid media, *J. Phys. Chem. A.*, 120 (2016) 6103-6110.  
<https://doi.org/10.1021/acs.jpca.6b03615>
- [7] R. Schmidt, C. Tanielian, R. Dunsbach, C. Wolff, Phenalenone, a universal reference compound for the determination of quantum yields of singlet oxygen  $O_2(^1\Delta_g)$  sensitization, *J. Photochem. Photobiol. A: Chem.* 79 (1994) 11-17. [https://doi.org/10.1016/1010-6030\(93\)03746-4](https://doi.org/10.1016/1010-6030(93)03746-4)



- [8] E. Oliveros, S.H. Bossmann, S. Nonell, C. Marti, G. Heit, G. Tröscher, A. Neuner, C. Martinez, A.M. Braun, Photochemistry of the singlet oxygen [ $O_2(^1\Delta_g)$ ] sensitizer perinaphtenone (phenalenone) in N,N'-dimethylacetamide and 1,4-dioxane, *New J. Chem.* 23 (1999) 85-93. <https://doi.org/10.1039/A804054K>
- [9] M. Segado, M. Reguero, Mechanism of the photochemical process of singlet oxygen production by phenalenone, *Phys. Chem. Chem. Phys.* 13 (2011) 4138-4148. <https://doi.org/10.1039/c0cp01827a>
- [10] J. Massiot, A. Makky, F. Di Meo, D. Chapron, P. Trouillas, V. Rosilio, Impact of lipid composition and photosensitizer hydrophobicity on the efficiency of light-triggered liposomal release, *Phys. Chem. Chem. Phys.*, 19 (2017) 11460-11473. <https://doi.org/10.1039/c7cp00983f>
- [11] I.O.L Bacillar, M.C. Oliveira, L.S. Dantas, E.B. Costa, H.C. Junqueira, W.K. Martins, A.M. Durantini, G. Cosa, P. Di Mascio, M. Wainwright, R. Miotto, R.M. Cordeiro, S. Miyamoto, M.S. Baptista, Photosensitized membrane permeabilization requires contact-dependent reactions between photosensitizer and lipids, *J. Am. Chem. Soc.* 140 (2018) 9606-9615. <https://doi.org/10.1021/jacs.8b05014>
- [12] J. Godard, D. Chapron, F. Brégier, V. Rosilio, V. Sol, Synthesis and supramolecular arrangement of new stearyl acid-based phenalenone derivatives, *Colloids Surf. A Physicochem. Eng. Asp.* 612 (2021b) 125988. <https://doi.org/10.1016/j.colsurfa.2020.125988>
- [13] J.F. Lovell, C.S. Jin, E. Huynh, H. Jin, C. Kim, J.L. Rubinstein, W.C.W. Chan, W. Cao, L.V. Wang, G. Zheng, Porphysomes nanovesicles generated by porphyrin bilayers for use as multimodal biophotonic contrast agents, *Nature Mat.*, 10 (2011) 324-332, <https://doi.org/10.1038/NMAT2986>.
- [14] J. Massiot, V. Rosilio, A. Makky, Photo-triggerable liposomal drug delivery systems: from simple porphyrin insertion in the lipid bilayer towards supramolecular assemblies of lipid-porphyrin conjugates, *J. Mater. Chem. B*, 7 (2019) 1805-1823, <https://doi.org/10.1039/c9tb00015a>.

- [15] E. Chang, J. Bu, J.W.H. Lou, M.S. Valic, M.H.Y. Cheng, V. Rosilio, J. Chen, G. Zheng, Porphyrin-lipid stabilized paclitaxel nanoemulsion for combined photodynamic therapy and chemotherapy, *J. Nanobiotechnol.*, 19 (2021) 154. <https://doi.org/10.1186/s12851-021-00898-1>
- [16] H.E. Jr Ries, H.D. Cook, Monomolecular films of mixtures. I. Stearic acid with isostearic acid and with tri-*p*-cresyl phosphate. Comparison of components with octadecylphosphonic acid and with tri-*o*-xenyl phosphate, *J. Colloid Interface Sci.*, 9 (1954) 535-546. [https://doi.org/10.1016/0095-8522\(54\)90056-2](https://doi.org/10.1016/0095-8522(54)90056-2)
- [17] P. Dynarowicz-Latka, V. Rosilio, P. Boullanger, P. Fontaine, M. Goldmann, A. Baszkin, Influence of a neoglycolipid and its PEO-lipid moiety on the organization of phospholipid monolayers, *Langmuir* 21 (2005) 11941-11948. <https://doi.org/10.1021/la051749w>
- [18] D. Chapron, J.-P. Michel, P. Fontaine, J. Godard, F. Brégier, V. Sol, V. Rosilio, Thermodynamic and structural properties of lipid-photosensitizer conjugates mixed with phospholipids: impact on the formation and stability of nanoassemblies, *Colloids Surf. B: Biointerfaces*, 231 (2023) 113565. <https://doi.org/10.1016/j.colsurfb.2023.113565>.
- [19] A. Hemmerle, N. Aubert, T. Moreno, P. Kékicheff, B. Heinrich, S. Spagnoli, M. Goldmann, G. Ciatto, P. Fontaine, Opportunities and new developments for the study of surfaces and interfaces in soft condensed matter at the SIRIUS beamline of Synchrotron SOLEIL, *J. Synchrotron Rad.* 31 (2024) 162-176. <https://doi.org/10.1107/S1600577523008810>
- [20] C. Fradin, A. Braslau, D. Luzet, D. Smilgies, M. Alba, N. Boudet, K. Mecke, J. Daillant, Reduction in the surface energy of liquid interfaces at short length scales, *Nature*, 403 (2000) 871-874. <https://doi.org/10.1038/35002533>
- [21] A. Dawiec, Y.-M. Abiven, D. Bachiller-Perea, J. Bisou, B. Kanoute, C. Meneglier, F. Orsini, Y. Sergent, G. Thibaux, Development of a new photon counting camera prototype for time resolved experiments at SOLEIL synchrotron, *AIP Conf. Proc.* 2054 (2019) 060067. <https://doi.org/10.1063/1.5084698>
- [22] J. Daillant, A. Gibaud. X-ray and neutron reflectivity: principles and applications. Springer, Berlin, 2009. <https://doi.org/10.1007/978-3-540-88588-7>

- [23] A. Glavic, M. Björck, GenX 3: the latest generation of an establish tool, *J. Appl. Cryst.* 55 (2022) 1063-1071. <https://doi.org/10.1107/S1600576722006653>
- [24] L. Berthelot, V. Rosilio, M.L. Costa, S. Chierici, G. Albrecht, P. Boullanger, A. Baszkin, Behavior of amphiphilic neoglycolipids at the air/solution interface. Interaction with a specific lectin, *Colloids Surf. B: Biointerfaces*, 11 (1998) 239-248. [https://doi.org/10.1016/S0927-7765\(98\)00043-5](https://doi.org/10.1016/S0927-7765(98)00043-5)
- [25] A. Ambike, V. Rosilio, B. Stella, S. Lepêtre-Mouelhi, P. Couvreur, Interaction of self-assembled squalenoyl gemcitabine nanoparticles with phospholipid-cholesterol monolayers mimicking a biomembrane, *Langmuir* 27 (2011) 4891-4899. <https://doi.org/10.1021/la200002d>.
- [26] M.-J. Hwang, K. Kim, Poly(ethylenimine) as a subphase stabilizer of stearic acid monolayers at the air/water interface: Surface pressure-area isotherm and infrared spectroscopy study, *Langmuir* 15 (1999) 3563-3569. <https://doi.org/10.1021/la9804029>
- [27] D. Risovic, S. Frka, Z. Kozarac, The structure of percolating lipid monolayers, *J. Colloid Interface Sci.* 373 (2012) 116. <https://doi.org/10.1016/j.jcis.2011.12.009>
- [28] L.T. Gew, M. Misran, Energetic mixing of anti-SNAP25 on lipid monolayers: degree of saturation of C18 fatty acids, *Surf. Interface Anal.* 49 (2017) 388-397. <https://doi.org/10.1002/sia.6144>
- [29] J.L.F. Rodriguez, L. Caseli, R.T. Rodrigues, J.M. Conde, P. Dynarowicz-Latka, Phase transition beyond the monolayer collapse – The case of stearic acid spread at the air/water interface, *Colloids Surf. A Physicochem. Eng. Asp.* 623 (2021) 126781. <https://doi.org/10.1016/j.colsurfa.2021.126781>
- [30] J.T. Koh, V.W. Cornish, P.G. Schultz, An experimental approach to evaluating the role of backbone interactions in proteins using unnatural amino acid mutagenesis, *Biochemistry* 36 (1997) 11314-11322. <https://doi.org/10.1021/bi9707685>
- [31] J. Mou, J. Yang, Z. Shao., Tri(hydroxymethyl)aminomethane (C<sub>4</sub>H<sub>11</sub>NO<sub>3</sub>) induced a ripple phase in supported unilamellar phospholipid bilayers, *Biochemistry* 33 (1994) 4439-4443.

<https://doi.org/10.1021/bi00181a001>

[32] L. Wolthaus, A. Schaper, D. Möbius, T.M. Jovin, Structural investigation of dipping lines in Langmuir-Blodgett films by scanning force microscopy, *Thin Solid Films* 242 (1994) 170-173. [https://doi.org/10.1016/0040-6090\(94\)90523-1](https://doi.org/10.1016/0040-6090(94)90523-1)

[33] S.E. Qaqish, M.F. Paige, Rippled domain formation in phase-separated mixed Langmuir-Blodgett films, *Langmuir* 24 (2008) 6146-6153. <https://doi.org/10.1021/la8002146> C

[34] A.F. Eftaiha, A.K. Qaroush, A.S. Abo-Shunnar, S.B. Hammad, K.I. Assaf, F.M. Ai-Qaisi, M.F. Paige, Interfacial behavior of modified nicotinic acid as conventional/gemini surfactants, *Langmuir* 38 (2022) 8524-8533. <https://doi.org/10.1021/acs.langmuir.2c00596>

[35] V. Dupres, S. Cantin, F Benhabib, F. Perrot, P. Fontaine, M. Goldmann, Two-dimensional mixtures of stearic acid and partially fluorinated amphiphilic molecule: A grazing incidence x-ray diffraction study, *Langmuir* 16 (2000) 10189-10192, <https://doi.org/10.1021/la000239t>

[36] V.M. Kaganer V.M., H. Möhwald, P. Dutta, Structure and phase transitions in Langmuir monolayers, *Rev. Mod. Phys.* 71 (1999) 779-819. <https://doi.org/10.1103/RevModPhys.71.779>.

[37] M.O. Sinnokrot, C.D. Sherrill, Substituent effects in  $\pi$ - $\pi$  interactions: Sandwich and T-shaped configurations, *J. Am. Chem. Soc.* 126 (2004) 7690-7697. <https://doi.org/10.1021/ja049434a>

[38] Michel J.P., Wang Y.X., Dé E., Fontaine P., Goldmann M., Rosilio V., Charge and aggregation pattern govern the interaction of plasticins with LPS monolayers mimicking the external leaflet of the outer membrane of Gram-negative bacteria, *Biochim. Biophys. Acta* 1848 (2015) 2967-2979. <http://dx.doi.org/10.1016/j.bbamem.2015.09.005>

[39] A. Botet-Carreras, M.T. Montera, O. Domènech, J.H. Borrell, Effect of cholesterol on monolayer structure of different acyl chained phospholipids, *Colloids Surf. B: Biointerfaces*, 174 (2019) 374-383. <https://doi.org/10.1016/j.colsurfb.2018.11.040>

## Supplementary information

### Impact of the nature of the linker on the 2D and 3D organization of lipid-phenalenone conjugates

David Chapron<sup>1,5</sup>, Jean-Philippe Michel<sup>1,5</sup>, Arnaud Hemmerle<sup>2</sup>, Philippe Fontaine<sup>2</sup>, Jeremy Godard<sup>3</sup>, Michel Goldmann<sup>4,2</sup>, Frédérique Brégier<sup>3</sup>, Vincent Sol<sup>3,5</sup>, Véronique Rosilio<sup>1,5\*</sup>

<sup>1</sup> Université Paris-Saclay, CNRS, Institut Galien Paris-Saclay, 17 avenue des Sciences, 91400 Orsay, France.

<sup>2</sup> Synchrotron SOLEIL, L'Orme des Merisiers, Départementale 128, 91190 Saint-Aubin, France.

<sup>3</sup> Univ. Limoges, LABCiS, UR 22722, 123 avenue Albert Thomas, 87000, Limoges, France.

<sup>4</sup> Institut des NanoSciences de Paris, CNRS, UMR 7588, Sorbonne Université, 4 place Jussieu, 75252 Paris cedex 05, France.

<sup>5</sup> CNRS, GDR 2025 HappyBio, Université d'Orléans, 14 rue d'Issoudun, BP 6744, 45067 Orléans cedex 2, France.

#### 1) Interfacial properties and morphology of conjugate monolayers

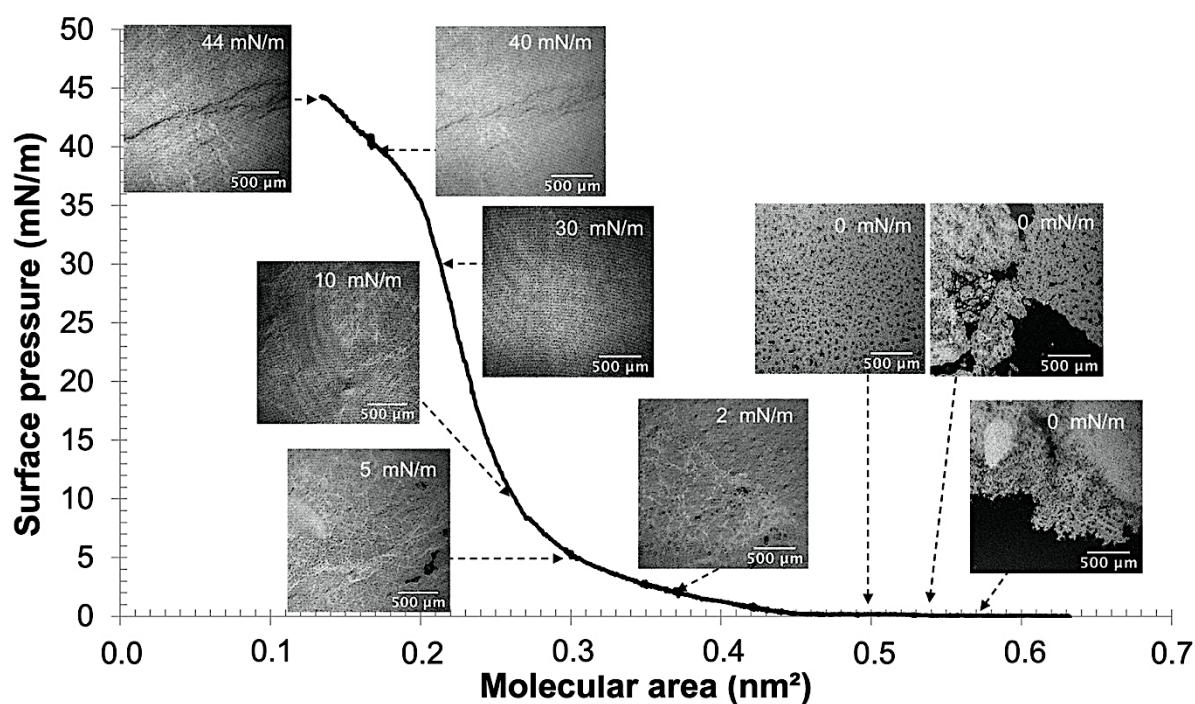


**Figure S1:**  $\pi$ -A isotherm and Brewster angle microscopy images for the monolayer of conjugate 1A spread at the air/water interface. Scale bar: 500  $\mu$ m.

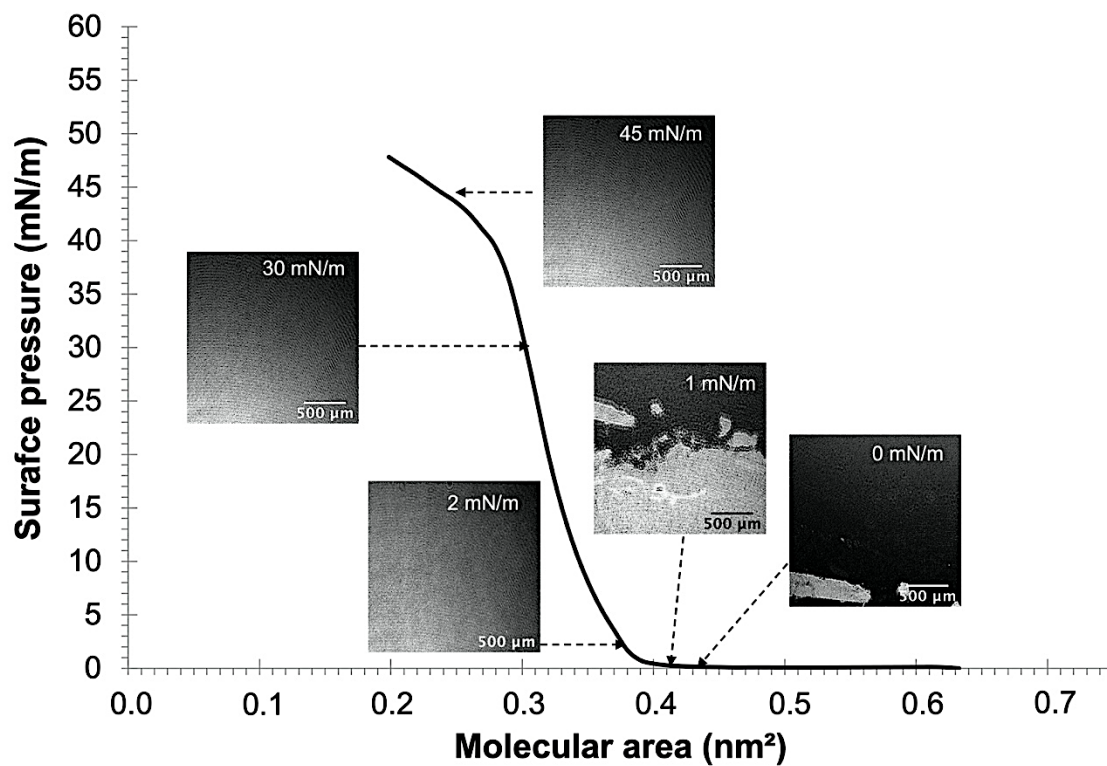


**Figure S2:**  $\pi$ -A isotherm and Brewster angle images for the conjugate **1B** monolayer at the air/water interface. Scale bar: 500  $\mu\text{m}$ .

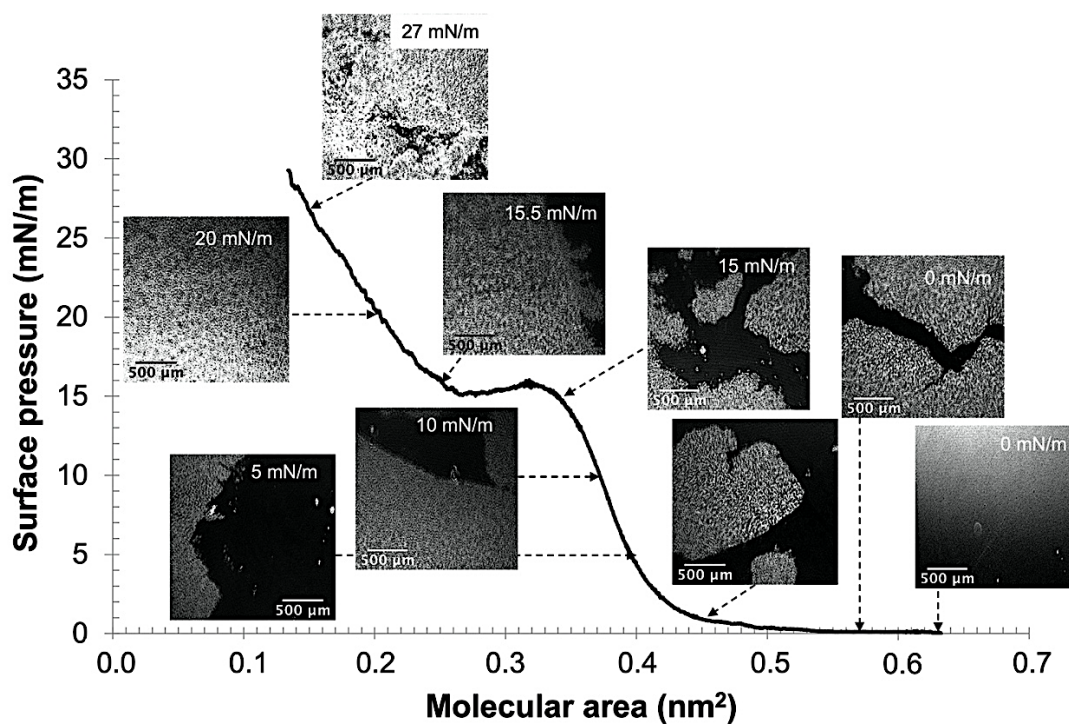


**Figure S3:**  $\pi$ -A isotherm and Brewster angle microscopy images for the monolayer of conjugate **1C** spread at the air/water interface. Scale bar: 500  $\mu\text{m}$ .

## 2) Possible conformations of conjugate 1B at the air-water interface

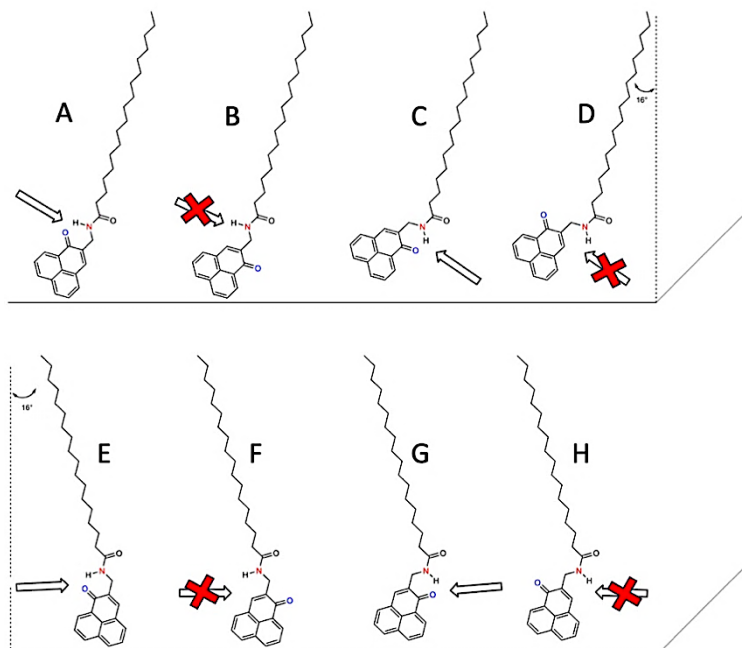


**Figure S4:** Possible conformations for conjugate **1B** at the air-water interface. The arrows indicate intramolecular H-bonding.  $R = C_{18}$ .

## 3) Interfacial properties and morphology of the conjugate 2 monolayer

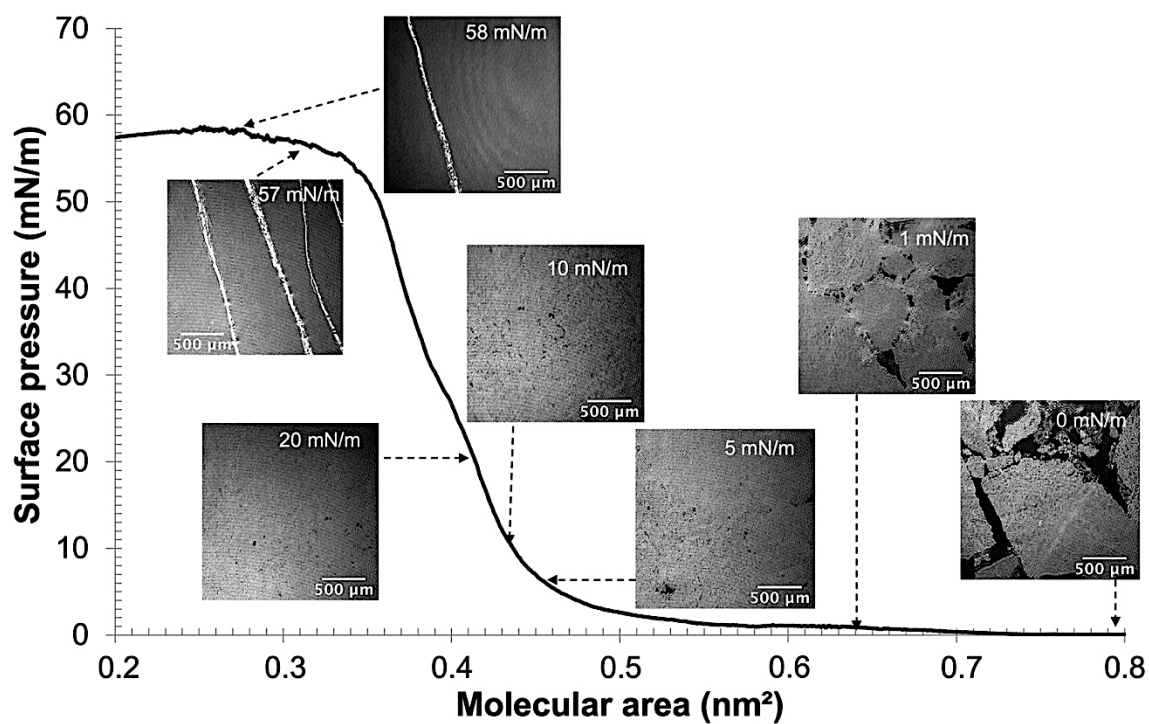


**Figure S5:**  $\pi$ -A isotherm and Brewster angle microscopy images showing the formation of conjugate **2** domains at the air/water interface during compression.

#### 4) GIXD and XRR parameters for the pure conjugates 1A, 1B, and 2.

**Table S1:** Bragg peak parameters (position Q, width W, and intensity I) extracted from GIXD spectra measured for pure conjugates **1A**, **1B**, and conjugate **2**, at increasing surface pressures. \*Bragg peaks [11] and [02] are degenerated above 30 mN/m surface pressure. ‘-’ denotes no diffraction signal.

| System                     | $\pi$ (mN/m)                               | 0            | 5            | 15            | 30            | 41            |
|----------------------------|--|--------------|--------------|---------------|---------------|---------------|
| <b>1A</b>                  | <b>Q<sub>02</sub> (nm<sup>-1</sup>)</b>    | <b>14.31</b> | <b>14.25</b> | <b>14.37</b>  | <b>14.31</b>  | <b>14.31</b>  |
|                            | W <sub>02</sub> (nm <sup>-1</sup> )        | 0.822        | 0.896        | 0.317         | 0.890         | 0.868         |
|                            | I <sub>02</sub> (counts)                   | 3949         | 4608         | 1757          | 3832          | 3447          |
|                            | <b>Q<sub>11</sub> (nm<sup>-1</sup>)</b>    | <b>15.63</b> | <b>15.44</b> | <b>15.19</b>  | <b>15.46</b>  | <b>15.41</b>  |
|                            | W <sub>11</sub> (nm <sup>-1</sup> )        | 0.860        | 1.101        | 1.20          | 1.045         | 1.053         |
|                            | I <sub>11</sub> (counts)                   | 1300         | 2872         | 3360          | 3182          | 3255          |
|                            | <b>Q<sub>side</sub> (nm<sup>-1</sup>)</b>  | <b>13.26</b> | <b>13.16</b> | <b>13.73</b>  | <b>13.20</b>  | <b>13.20</b>  |
|                            | W <sub>side</sub> (nm <sup>-1</sup> )      | 0.429        | 0.101        | 0.690         | 0.259         | 0.167         |
| I <sub>side</sub> (counts) | 837  | 690          | 1656         | 427           | 471           |               |
| System                     | $\pi$ (mN/m)                               | 0            | 5            | 15            | 30            | 35            |
| <b>1B</b><br>Chains        | <b>Q<sub>11</sub> (nm<sup>-1</sup>)</b>    | -            | <b>13.55</b> | <b>13.52</b>  | <b>13.66</b>  | <b>13.75</b>  |
|                            | W <sub>11</sub> (nm <sup>-1</sup> )        | -            | 0.245        | 0.288         | 0.262         | 0.396         |
|                            | I <sub>11</sub> (counts)                   | -            | 2780         | 3217          | 2945          | 737           |
|                            | <b>Q<sub>02</sub> (nm<sup>-1</sup>)</b>    | -            | <b>14.03</b> | <b>14.06</b>  | <b>14.08</b>  | <b>14.14</b>  |
|                            | W <sub>02</sub> (nm <sup>-1</sup> )        | -            | 0.127        | 0.140         | 0.188         | 0.355         |
|                            | I <sub>02</sub> (counts)                   | -            | 8712         | 8984          | 9974          | 5610          |
| <b>1B</b><br>Polar head    | <b>Q<sub>02</sub> (nm<sup>-1</sup>)</b>    | -            | <b>17.45</b> | <b>17.46</b>  | <b>17.52</b>  | <b>17.47</b>  |
|                            | W <sub>02</sub> (nm <sup>-1</sup> )        | -            | 0.234        | 0.232         | 0.264         | 0.439         |
|                            | I <sub>02</sub> (counts)                   | -            | 3874         | 4663          | 5090          | 3192          |
|                            | <b>Q<sub>10</sub> (nm<sup>-1</sup>)</b>    | -            | <b>18.46</b> | <b>18.48</b>  | <b>18.53</b>  | <b>18.58</b>  |
|                            | W <sub>10</sub> (nm <sup>-1</sup> )        | -            | 0.499        | 0.500         | 0.500         | 0.500         |
|                            | I <sub>10</sub> (counts)                   | -            | 1813         | 2154          | 2342          | 1651          |
| System                     | $\pi$ (mN/m)                               | 5            | 15           | 30            | 40            | 45            |
| <b>2</b>                   | <b>Q<sub>11/02</sub> (nm<sup>-1</sup>)</b> | <b>15.11</b> | <b>15.20</b> | <b>15.23*</b> | <b>15.25*</b> | <b>15.27*</b> |
|                            | W <sub>11/02</sub> (nm <sup>-1</sup> )     | 0.170        | 0.151        | 0.160         | 0.150         | 0.157         |
|                            | I <sub>11/02</sub> (counts)                | 27637        | 34369        | 33235         | 33347         | 32381         |

**Table S2:** Characteristic GIXD parameters for pure conjugate **2**, conjugates **1B** and **1A**. a, b: lattice parameters, A=ab: area of the unit cell, t tilt, L<sub>xy</sub>=2/w: correlation length. \*Values measured at 35mN/m.

| System              | $\pi$ (mN/m)         | 0     | 5     | 15    | 30    | 40     | 45    | Tilt orientation         |
|---------------------|----------------------|-------|-------|-------|-------|--------|-------|--------------------------|
| <b>1A</b>           | A (nm <sup>2</sup> ) | 0.494 | 0.501 | 0.496 | 0.497 | 0.497* | -     | R<br>NNN                 |
|                     | a (nm)               | 0.563 | 0.568 | 0.568 | 0.566 | 0.566* | -     |                          |
|                     | b (nm)               | 0.880 | 0.882 | 0.874 | 0.878 | 0.880* | -     |                          |
|                     | Tilt t (°)           | 28.1  | 29.1  | 29.1  | 29.3  | 27.0*  | -     |                          |
|                     | L <sub>xy</sub> (nm) | 2.4   | 2.3   | 2.9   | 2.3   | 2.3*   | -     |                          |
| <b>1B</b><br>Chains | A (nm <sup>2</sup> ) | -     | 0.485 | 0.486 | 0.479 | 0.474  | -     | R<br>NNN                 |
|                     | a (nm)               | -     | 0.542 | 0.544 | 0.537 | 0.533  | -     |                          |
|                     | b (nm)               | -     | 0.895 | 0.894 | 0.892 | 0.889  | -     |                          |
|                     | Tilt t (°)           | -     | 15.3  | 15    | 15.8  | 16.2   | -     |                          |
|                     | L <sub>xy</sub> (nm) | -     | 15.7  | 14.3  | 10.6  | 5.6    | -     |                          |
| <b>2</b>            | A (nm <sup>2</sup> ) | -     | 0.399 | 0.395 | 0.393 | 0.392  | 0.391 | Negligible<br>or no tilt |
|                     | a (nm)               | -     | 0.480 | 0.477 | 0.476 | 0.476  | 0.475 |                          |
|                     | b (nm)               | -     | 0.832 | 0.828 | 0.825 | 0.824  | 0.823 |                          |
|                     | Tilt t (°)           | -     | 0.3   | 0     | 0     | 0      | 0     |                          |
|                     | L <sub>xy</sub> (nm) | -     | 11.7  | 13.2  | 12.5  | 13.3   | 12.7  |                          |
|                     | Symmetry             | -     | R     | R     | H     | H      | H     |                          |



**Table S3:** Fitted values and errors obtained for each sublayer (chain or polar head) composing the phenalene derivative layer studied by reflectometry at the air/water interface.

|                             | <b>Conjugate 1A</b><br>$\pi = 5 \text{ mN/m}$ | <b>Conjugate 1B</b><br>$\pi = 5 \text{ mN/m}$ | <b>Conjugate 2</b><br>$\pi = 5 \text{ mN/m}$ |
|-----------------------------|---|---|--|
| Chain thickness (nm)        | $1.35 \pm 0.13$                               | $1.43 \pm 0.17$                               | $2.31 \pm 0.14$                              |
| Chain roughness (nm)        | $0.61 \pm 0.12$                               | $0.31 \pm 0.11$                               | $0.46 \pm 0.07$                              |
| Head thickness (nm)         | $1.25 \pm 0.25$                               | $0.66 \pm 0.12$                               | $0.66 \pm 0.07$                              |
| Head roughness (nm)         | $0.80 \pm 0.14$                               | $0.4 \pm 0.21$                                | $0.68 \pm 0.07$                              |
| <b>Total thickness (nm)</b> | <b><math>2.6 \pm 0.28</math></b>              | <b><math>2.09 \pm 0.21</math></b>             | <b><math>2.97 \pm 0.16</math></b>            |

|                             | <b>Conjugate 1A</b><br>$\pi = 40 \text{ mN/m}$ | <b>Conjugate 1B</b><br>$\pi = 40 \text{ mN/m}$ | <b>Conjugate 2</b><br>$\pi = 40 \text{ mN/m}$ |
|-----------------------------|--|--|---|
| Chain thickness (nm)        | $1.76 \pm 0.18$                                | $1.42 \pm 0.06$                                | $2.18 \pm 0.04$                               |
| Chain roughness (nm)        | $0.65 \pm 1.7$                                 | $0.43 \pm 0.06$                                | $0.5 \pm 0.07$                                |
| Head thickness (nm)         | $1.25 \pm 0.3$                                 | $0.95 \pm 0.12$                                | $1.1 \pm 0.1$                                 |
| Head roughness (nm)         | $0.80 \pm 0.31$                                | $0.41 \pm 0.1$                                 | $0.17 \pm 0.18$                               |
| <b>Total thickness (nm)</b> | <b><math>3.01 \pm 0.35</math></b>              | <b><math>2.37 \pm 0.13</math></b>              | <b><math>3.23 \pm 0.11</math></b>             |

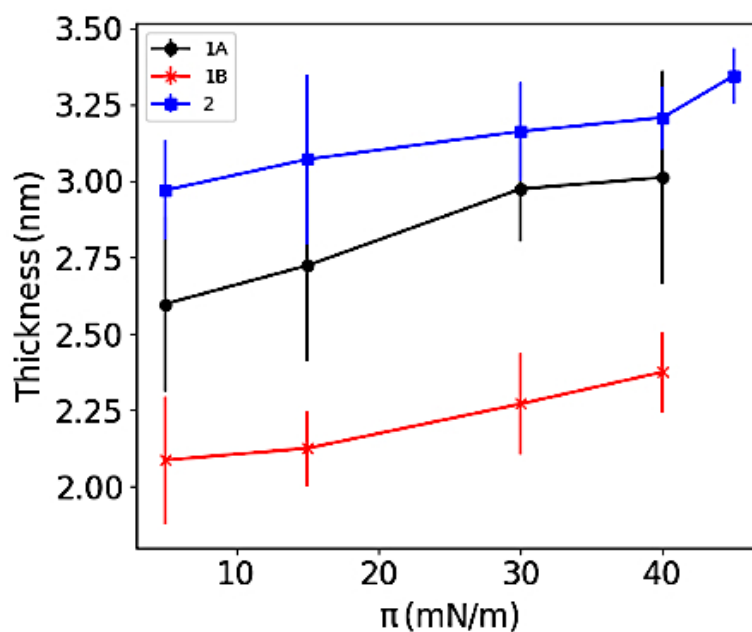


**Figure S6:** Evolution of the total thickness of each layer with the surface pressure as obtained by fits of the XRR data.

## 5) Morphology of nano-assemblies made of conjugates 1A, 1B, and 2.

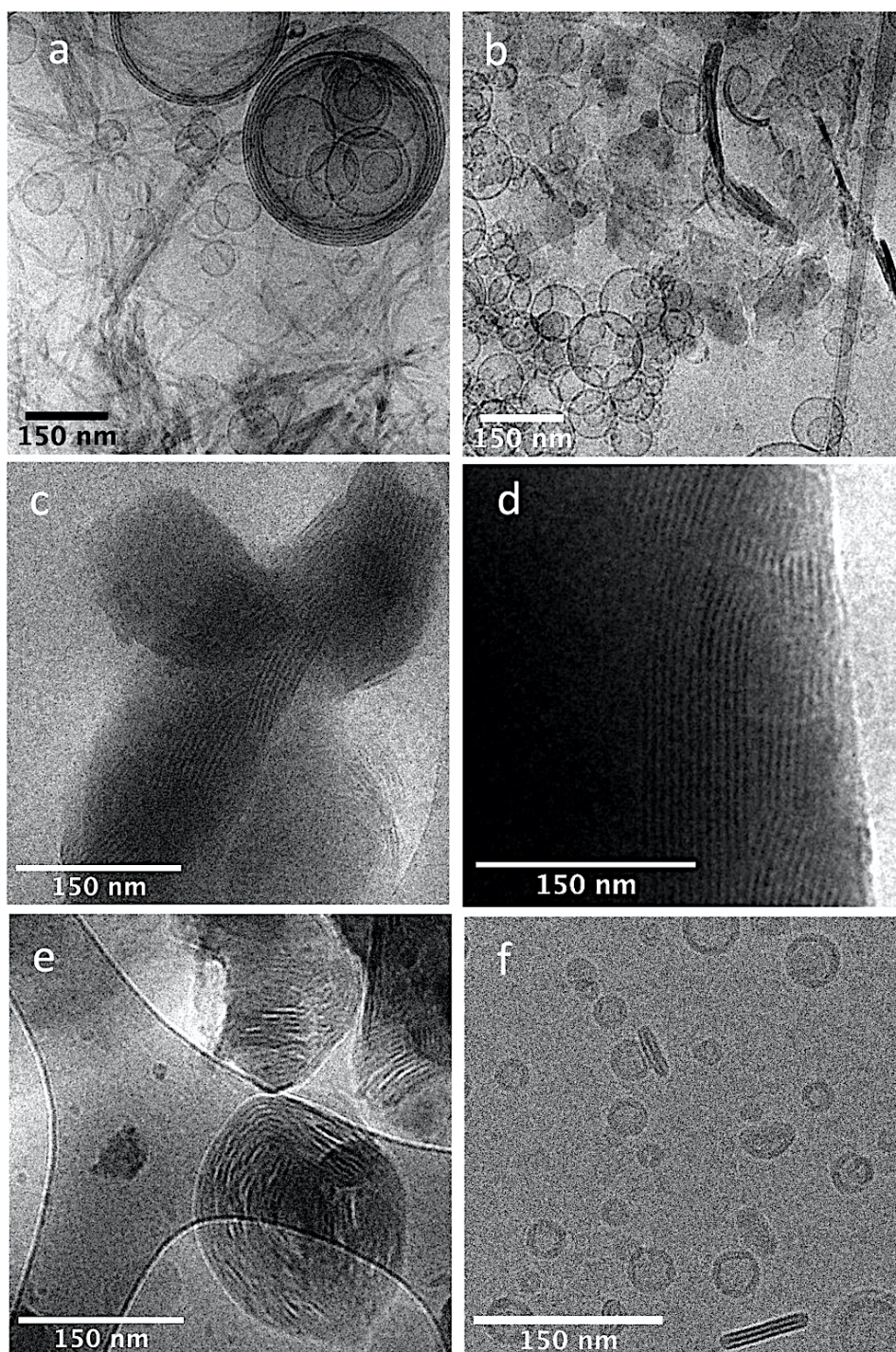


**Figure S7:** CryoTEM images showing the morphology of nano-assemblies formed with stearyl-oleoyl phosphatidylcholine (SOPC) and conjugates **1A** (a) at 10 mol%, **1B** (b) at 40 mol%, and conjugate **2**, pure (c,d,e) or mixed with SOPC (f, 50 mol%). CryoTEM conditions are described in Godard *et al.* and Chapron *et al.*

**J. Godard *et al.*** Colloids Surf. A Physicochem. Eng. Asp. 612 (2021) 125988. <https://doi.org/10.1016/j.colsurfa.2020.125988>. **D. Chapron *et al.*** Colloids Surf. B: Biointerfaces, 231 (2023) 113565. <https://doi.org/10.1016/j.colsurfb.2023.113565>.